THESIS

OBSERVED STRUCTURE, EVOLUTION AND POTENTIAL INTENSITY OF CATEGORY FIVE HURRICANE ISABEL (2003) FROM 12 – 14 SEPTEMBER

Submitted by

Michael Monroe Bell

Department of Atmospheric Science

In partial fulfillment of the requirements

For the Degree of Master of Science

Colorado State University

Fort Collins, Colorado

Summer 2006

COLORADO STATE UNIVERSITY

April 17, 2006

WE HEREBY RECOMMEND THAT THE THESIS PREPARED UNDER OUR SUPERVISION BY MICHAEL MONROE BELL ENTITLED OBSERVED STRUCTURE, EVOLUTION AND POTENTIAL INTENSITY OF CATEGORY FIVE HURRICANE ISABEL (2003) FROM 12 – 14 SEPTEMBER BE ACCEPTED FOR FULFILLING IN PART REQUIREMENTS FOR THE DEGREE OF MASTER OF SCIENCE.

Committee on Graduate work

_____
Outside Committee Member, Dr. Michael Kirby

_____
Committee Member, Dr. Wen-Chau Lee

_____
Committee Member, Dr. Richard Johnson

_____
Adviser, Dr. Michael Montgomery

_____
Department Head/Director, Dr. Steven Rutledge

ABSTRACT OF THESIS

OBSERVED STRUCTURE, EVOLUTION, AND POTENTIAL INTENSITY OF CATEGORY FIVE HURRICANE ISABEL (2003) FROM 12 – 14 SEPTEMBER

Unprecedented observations of Hurricane Isabel (2003) at category five intensity were collected from 12 – 14 September as part of the Coupled Boundary Layer Air-Sea Transfer (CBLAST) field experiment. This study presents what is believed to be the first detailed analysis of the sea surface temperature, outflow layer, atmospheric boundary layer, and inner-core structure of a *superintense* tropical cyclone using high resolution in situ flight level, NCAR GPS dropwindsonde, Doppler radar, and satellite measurements. The analysis of the dropwindsonde and in-situ data includes a comprehensive discussion of the uncertainties associated with this observational dataset and provides an estimate of the storm-relative axisymmetric inner-core structure using Barnes objective analysis. Though Barnes objective analysis has been used extensively with synoptic and satellite data, its application for inferring radius-height mean hurricane structure is believed to be novel. An assessment of gradient and thermal wind balance in the inner core is also presented, as well as the examination of an extreme 107 m s^{-1} wind speed measurement obtained on the 13^{th}.

The axisymmetric data composites presented in this study suggest that Isabel built a reservoir of high moist entropy air inside the low-level eye between 12 and 13 September, which was then utilized as an additional energy source to nearly maintain its extreme intensity through the 14^{th} even after crossing the cool wake of Hurricane Fabian. It is argued here that there is significant penetration of near-surface air from the inflow

that replenishes the air mixed out of the eye. This inflowing air is enhanced thermodynamically, acquiring additional entropy through interaction with the ocean. The combined mean and asymmetric eddy flux of high moist entropy air from the low-level eye into the eyewall represents an additional power source, or "turbo-boost" to the hurricane heat engine. Recent estimates of the ratio of sea-to-air enthalpy and momentum exchange at high wind speed from CBLAST are used to suggest that Isabel utilized this extra power to exceed the previously assumed intensity upper bound for the given environmental conditions on all three days. This discrepancy between *a priori* maximum potential intensity theory and observations is as high as 10 – 35 m s^{-1} on 13 September, providing observational validation of recent numerical and theoretical work along with new scientific challenges and practical implications for the current understanding of hurricanes.

Michael Monroe Bell
Atmospheric Science Department
Colorado State University
Fort Collins, CO 80523
Summer 2006

Acknowledgements

My deepest thanks go to my advisor, Professor Michael Montgomery, and my NCAR supervisor, Wen-Chau Lee for their expertise, motivation, and enthusiasm during the course of this research. I would also like to extend my sincere gratitude to my beautiful wife Jennifer and daughter Lucerne for their support while completing my coursework and this research. Special thanks go to Michael Black for getting Prof. Montgomery a seat aboard NOAA 43 on the 13 September mission into Hurricane Isabel from which this study grew, for getting me on the NOAA 42 mission into Hurricane Rita on 22 September 2005, and his helpful comments throughout the research process as well. Many thanks to Sim Aberson for his assistance and analysis of the 'supersonde' presented in Chapter 4. I would also like to thank my committee members, Professors Richard Johnson and Michael Kirby for their helpful comments.

I would like to acknowledge NCAR/EOL for their support of this degree, NOAA/NESDIS for their support of the Ocean Winds Experiment; NOAA and ONR for supporting the CBLAST experiment from which these data were obtained; and the pilots and support crew of the NOAA-P3 and U.S. Air Force aircraft for their bravery and dedication to hurricane science and forecasting. Dropwindsonde data were processed by Krystal Valde, Bill Ramstrom, and Steven Feuer. I would like to thank Pete Black, Frank Marks, Ed Zipser, John Persing, Russ Elsberry, Scott Braun, Kerry Emanuel, and Tim Dunkerton. This research was funded in part by ONR Grant N00014-02-1-0474, and NSF Grants NSF-ATM-0132006, NSF-ATM-0101781, and NSF-ATM-0349980.

Table of Contents

List of Figures

wind, the shorter dashed curve the radial wind, and the longer dashed curve the difference between the balanced and nonbalanced wind. Wind components are nondimensionalized with the maximum balanced wind, and radius is nondimensionalized with the radius of maximum balanced wind.

7.1 SST derived from AVHHR satellite (average SST over 04 to 10 September in color), and NOAA WP-3D downward-pointing radiometer (thin line, from ~18Z 13 and 14 September). Tracks of Hurricanes Fabian (dashed best track, from 02 to 05 September) and Isabel (dashed best track, with thick white, solid line indicating analysis periods from 16 – 23Z on 12 to 14 September) are shown for reference.

7.2 (a) GOES infrared satellite imagery at 2215 UTC (courtesy of NRL/Monterey) showing extent of hurricane outflow, and the dropwindsonde profile locations (red dots with UTC time labels) used in outflow temperature calculation. 'X' indicates location of additional outflow jet sample at 553 km radius from center, (b) High altitude wind speed (ms^{-1}) and θ_e (K) from NOAA Gulfstream-IV dropwindsonde at 341 km radius from center at 2227 UTC. Tangential (red) and radial (blue) winds show anticyclonic outflow, with θ_e in green. Black dashed line indicates linearly interpolated data.

7.3 GOES infrared satellite imagery (courtesy of NRL/Monterey) at (a) 12/2045 UTC and (b) 14/2145Z showing extent of hurricane outflow, and the dropwindsonde profile locations (red dots with UTC time labels) used in outflow temperature calculation.

7.4 Ratio of Dalton number (enthalpy exchange coefficient) to drag coefficient derived from CBLAST measurements (circles with vertical lines indicating standard error) as well as an average of prior values below 20 m/s from HEXOS (DeCosmo et al., 1996; Smith et al, 1992, dashed line) and TOGA-COARE 3.0 (Fairall et al 2003, solid line). Estimated value based on budget estimate (Emanuel, 2004) at winds near 70 m/s is shown with a square. Interpolated estimates from Fairall estimate of spray effects shown with asterisks. The thin horizontal line is the 0.75 threshold for TC development proposed by Emanuel, 1996. [From Black et al, 2006]

7.5 Photograph of sea surface in Hurricane Isabel taken from NOAA 43 during stepped descent pattern below 400 m altitude. Surface wind speed is 20 – 30 m s-1. [Photo courtesy Michael Black]

7.6 Theoretically predicted azimuthal mean V_{max} at the boundary layer top for varying outflow temperature and near-core SST with a constant RH = 80%. 'X' indicates the primary potential intensity estimate for the observed near environment around Isabel (using 27.5 ˚C SST near eyewall region associated with Fabian's wake), yielding a 56.6 ms^{-1} mean V_{max}. The dark solid curve represents the average storm-relative tangential wind speed at the top of the boundary layer derived from the dropwindsonde measurements. The shading represents the 6 ms^{-1} standard deviation of this mean value. This *a priori* E-MPI estimate assumes C_K/C_D =1. See text for assumptions leading to upper and lower bound estimates.

List of Tables

Chapter 1

Introduction

Category five and supertyphoon[1] class tropical cyclones (TCs) are one of the most awe-inspiring natural phenomena on the planet. Their savage beauty and tremendous power have had profound impacts on history (Emanuel, 2005). These relatively rare phenomena have the potential damage of 500 times that of a category one storm (Pielke and Landsea, 1998), challenging the limits of even the most extreme structural engineering. Meteorological observations from storms that achieve this infamous status provide a glimpse at the hurricane heat engine operating at peak efficiency, yielding new insights into the thermomechanics of TCs.

One goal towards a complete understanding of hurricane intensity is an accurate theory that predicts a reasonable upper limit of intensification, or the maximum potential intensity (MPI), of a TC for a given set of environmental conditions. MPI theory not only provides a prediction of the capability for a storm to achieve category five, but also a simplified framework in which to study the processes that drive the hurricane engine. Understanding intensity change then becomes a matter of accurately determining the limiting factors that prevent a TC from realizing and/or maintaining its peak intensity and efficiency.

[1] Category five refers to the highest level on the Saffir-Simpson scale used in the Atlantic basin. Supertyphoon is a term used in the Western Pacific basin used to describe major hurricanes, and is roughly equivalent to category four or higher in the Atlantic basin.

One approach to MPI is to use statistical predictors, such as the work of DeMaria and Kaplan (1994). As a testament to the difficulty in forecasting TC intensity, statistical models currently show more skill than some operational dynamical models (DeMaria et al. 2005). Statistical MPI provides an important empirical upper-limit for intensity, and verification of the importance of environmental parameters that are favorable for development, but it has little to say about the processes that control TC intensity. More comprehensive MPI theories have therefore been advanced and refined over the last few decades that are based on simplified dynamical and thermodynamical arguments (Camp and Montgomery 2001). These MPI theories predict the upper bound for hurricane intensity based on the energetics and dynamics of the atmosphere-ocean system, and should be valid for a complete set of environmental conditions. Significant violations of the predicted upper intensity over and above observational error are therefore not simply statistical anomalies, but indications that the dynamical basis of the theory is either flawed or incomplete.

Previous studies have attempted to test various MPI theories using numerical models (Rotunno and Emanuel 1987; Persing and Montgomery 2003, hereafter PM03), East Pacific environmental soundings (Hobgood 2003), and best track and satellite datasets (Tonkin et al. 2000). A critical limitation to testing the limits of MPI theory is the lack of detailed observations in category five tropical cyclones. Even with operational aircraft reconnaissance, it is difficult to establish high-resolution two or three-dimensional structure of a hurricane (Hawkins and Rubsam, 1964; Hawkins and Imbembo, 1976). Intensive observing periods (IOPs) conducted as part of a dedicated field project are an effective, and often only, way to obtain the quantity and quality of

observations needed to adequately test meteorological theory. Three IOPs into Hurricane Isabel were obtained during the Coupled Boundary Layer Air-Sea Transfer (CBLAST) field campaign from 12 - 14 September, 2003 while she was at category five intensity. The Office of Naval Research (ONR) sponsored this experiment in order to more accurately measure, understand and parameterize air-sea fluxes in the hurricane environment (Black et al. 2006). These fluxes are a critical component of MPI theories proposed by Kleinschmidt 1951, hereafter K51), Malkus and Riehl (1960, hereafter MR60), and Emanuel and colleagues (Emanuel 1986; Rotunno and Emanuel 1987; Emanuel 1988; 1991; 1995; 1997; Bister and Emanuel 1998; Emanuel et al. 2004; hereafter referred to as E-MPI). The complex nature and behavior of the ocean surface at high wind speeds is one of the least understood aspects of hurricane science. This is illustrated in Fig 1.1 with a photograph of the sea surface underneath the eyewall of Hurricane Gilbert (1998). The sharp delineation of the spray layer as one approaches the eyewall transforms into a region of violent turbulence where the distinction between air and sea becomes difficult, if not impossible to define. The CBLAST field program directly measured the bulk enthalpy and momentum exchange coefficients used to parameterize this complex air-sea interaction at the highest wind speeds to date.

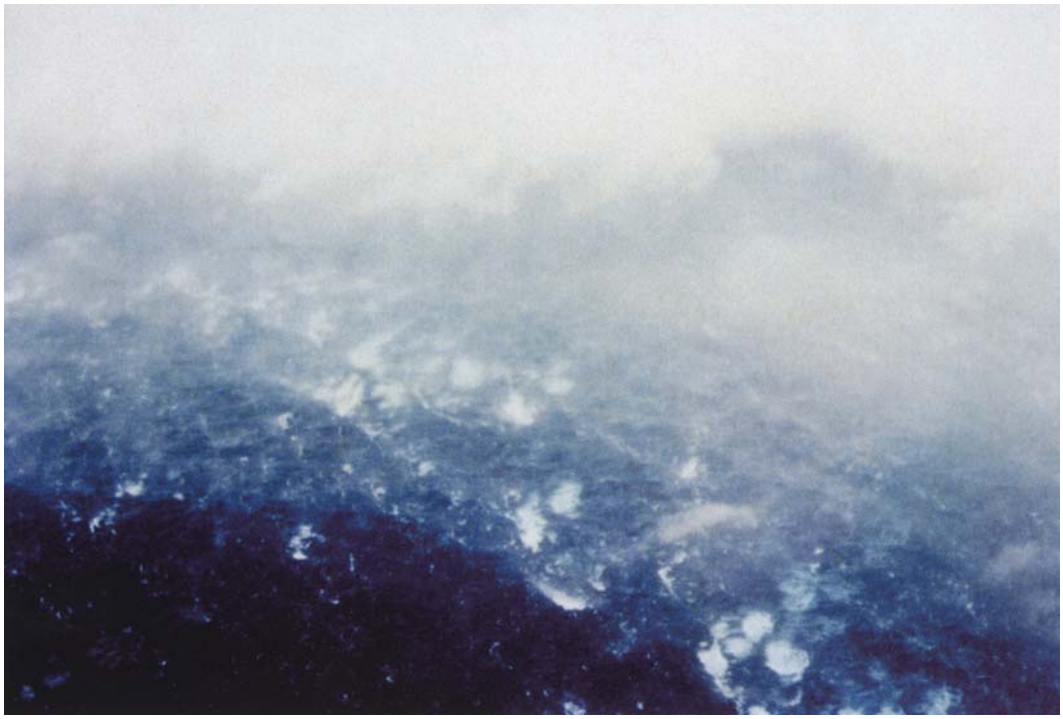

Figure 1.1 The sea state under the eyewall of an intense hurricane may be gleaned from this remarkable photograph of the inner edge of the eyewall of Hurricane Gilbert of 1988. The center of the vortex is in the lower left of this picture. [From Emanuel, 2005]

This dataset provides a unique opportunity to use detailed *in-situ* observations of the sea surface temperature, outflow layer, atmospheric boundary layer, and inner-core structure to test the limits and predictions of MPI theory, and examine the structure and balance of the hurricane engine operating at near peak efficiency. This study attempts to accurately quantify the environmental parameters used in the E-MPI formulation using measurements obtained during the CBLAST field campaign, and compare the resulting maximum intensity predictions with the observed intensity of a category five TC. This theory predicts an upper bound on the mean tangential wind at the swirling boundary layer top for given environmental conditions. Hurricane Isabel is found to exceed this upper bound on three consecutive days from 12 – 14 September 2003, and provides the

first evidence for the existence of *superintense* storms in nature that were previously predicted using high-resolution computer simulations (PM03).

The in-situ observations of equivalent potential temperature (θ_e) and radial wind analyzed here suggest that Isabel built a reservoir of high entropy air in the low-level eye between the 12th and 13th, and that significant penetration of near-surface air from the inflow on the 13th was enhanced thermodynamically, acquiring the characteristics of the high entropy air in the eye. This low-level inflow replenishes the air mixed out of the eye, and provides additional power to the hurricane engine by injection into the eyewall cloud. The eye dynamics can therefore be likened to a "second-cycle" of the Carnot engine, in which thermodynamic energy drawn from the underlying ocean within the eye augments the energy obtained from the ocean underneath and outside the eyewall, where current theory assumes all of the energy uptake occurs (e.g., Emanuel 1997). It is suggested that the high entropy air in the low-level eye was utilized as an energy source to nearly maintain its extreme intensity through the 14th, even after crossing the cool wake of Hurricane Fabian.

Chapter 2 provides a brief review of several MPI theories and recent studies that have tested them. Chapter 3 details the dataset and analysis methodology used in this study. The evolution of Isabel's axisymmetric structure from the 12th to the 14th is presented in chapter 4, including some of the highest resolution potential vorticity fields of the hurricane inner core derived from observational data to date. Some observations of smaller scale features, including the strongest recorded wind speed in an Atlantic TC, are presented in chapter 5. An analysis of gradient and thermal wind balance is given in

chapter 6. Observed environmental conditions and E-MPI predictions are shown in chapter 7, followed by conclusions and summary.

Chapter 2

Maximum Potential Intensity Theory

2.1 Review of MPI Theories

Early theoretical work on hurricane intensity by K51, MR60, Miller (1958), and Carrier et al. (1971) emphasized different aspects of the MPI problem. A central difference in these theories was the importance of the oceanic energy source. Carrier et al. (1971) considered the problem to be fundamentally based on mid-tropospheric dynamics, and had limited thermodynamic contribution from the ocean in their theory. Miller (1958) considered the sea surface temperature (SST) to be of importance in providing the thermodynamic structure for an air parcel that is lifted moist adiabatically in the eyewall and subsequently sinks to the surface in the eye, warming dry adiabatically. This 'two-cell' trajectory model therefore depends heavily on the presence of environmental convective available potential energy (CAPE). Miller's theory was later expanded by Holland (1997, hereafter H-MPI) to account for the pressure dependence of equivalent potential temperature (θ_e). A pressure fall in the eyewall leads to an increase in boundary layer θ_e, resulting in a convectively unstable parcel near the ocean surface. This parcel then rises moist adiabatically in the eyewall, warming the atmospheric column and leading to an additional, smaller pressure drop. This process is repeated until a convergent solution is obtained, yielding the surface pressure under the eyewall for a given environmental sounding. A parameterized eye sounding can be constructed if the

pressure fall beneath the eyewall is greater than 20 hPa, and additional iterations then yield the minimum central pressure of the TC.

H-MPI has a strong dependence on the available CAPE in an environmental sounding, but has no consideration of frictional dissipation or enthalpy fluxes from the ocean surface. While ambient CAPE is clearly important in supporting tropical convection, the role of the quantity as a predictive parameter for TC potential intensity is questionable. Camp and Montgomery (2001) showed that soundings with large amounts of CAPE over moderately warm ocean surfaces could lead to extremely low central pressures in H-MPI, potentially violating the 'reasonableness' assumption of a proper MPI theory. While such a 'hypercane' parameter regime also exists in E-MPI, the conditions supporting such ferocious storms do not currently exist on Earth, whereas H-MPI superstorms are potentially found within common late summer sea surface temperature regimes around 29 C. Persing and Montgomery's (2005) modeling results further suggest that ambient convective instability is consumed quickly by a storm and thereafter plays a minor role in the maximum intensity of a tropical cyclone. Additionally, for the purposes of this study, H-MPI offers only a prediction for central pressure and not for wind speed. Since pressure-wind relationships are dependent on storm size, intensity, and motion (Callaghan and Smith, 1998), conversion between the two intensity measures may introduce some ambiguity and is not considered here.

The work of Kleinschmidt (1951) introduced the idea of an energy balance between the amount of sensible and latent heat a TC can extract from the ocean surface and the momentum lost to the sea through frictional dissipation. A steady-state TC at maximum intensity maintains this balance exactly, and the MPI is therefore a function of

the energy change of a parcel as it spirals into the eyewall in the boundary layer. The addition of heat and moisture to the hurricane engine from the ocean is one of the central aspects of the K51, MR60, and E-MPI theories that distinguish them from Miller (1958) and H-MPI. Since the amount of energy added to a TC in an approximately isothermal boundary layer is proportional to the change in (moist) entropy, the radial structure of boundary-layer θ_e plays a critical role in determining the maximum intensity of a TC in these theories.

Kleinschmidt did not pursue a formal *a priori* MPI theory, but rather attempted to explain the structure of a steady-state intense TC whose core θe was approximately known (Camp, 2000). Malkus and Riehl (1960) presented an MPI theory based on the concept of energy balance similar to that of K51, and they were the first to derive an expression for the maximum tangential wind of a TC given the *a priori* SST, air temperature, and bulk heat and momentum exchange coefficients. While they acknowledge the importance of latent heat fluxes from the sea surface, the bulk moisture exchange coefficient was not explicitly taken into account in their equation for maximum tangential wind. One crucial assumption that stands in contrast to E-MPI was that nearly all of a parcel's energy (moist entropy) gain is obtained on its inward spiral from the outer core, as opposed to directly underneath the eyewall. Thus, one would expect to see a large $\delta\theta_e$ from the outer core to the eyewall if this assumption were correct. This differs from E-MPI in that Emanuel assumes that the strongest enthalpy fluxes are collocated with the highest wind speeds, and hence are found at the base of the eyewall.

Since the pioneering paper by Emanuel (1986), the wind-induced surface heat exchange (WISHE) model for tropical cyclone intensification has been largely accepted

in the hurricane community as a paradigm. The WISHE instability is a mechanism by which an initial vorticity disturbance can grow over a warm ocean, with increasing wind speeds providing a positive feedback cycle that is able to extract increasing amounts of moist entropy from the ocean surface. The end result is a steady-state balance between the amount of energy obtained from the ocean and that dissipated by friction in the boundary layer, similar to that presented by K51 and MR60. Another key aspect of E-MPI, shared with K51, is the assumption that CAPE generated by increased boundary layer θe is extinguished quickly, returning the atmosphere to a state of convective neutrality.

Though E-MPI theory has been revised over the years to include improved eye parameterization (1995a), turbulent dissipative heating (Bister and Emanuel 1998), and ocean cooling feedbacks (Emanuel et al. 2004), the central concept of the hurricane as Carnot engine has proven both useful and largely accurate. This concept is illustrated in Figure 2.1, showing an idealized representation of the TC secondary circulation. As an air parcel moves radially inward to the eyewall, it is in contact with the warm, moist ocean surface and obtains energy from this heat reservoir analogously to an isothermal expansion leg of the Carnot cycle. At the base of the eyewall, a parcel rises and expands moist adiabatically, releasing the latent heat acquired from the ocean and dropping the pressure of the cyclone. The parcel then is then ejected from the TC in the upper-tropospheric outflow layer, where it radiates excess energy to space and sinks. This is analogous to the Carnot isothermal compression leg in response to a cool reservoir. The final leg of a parcel is adiabatic compression and return to the boundary layer, where the simplified model repeats. Thus, the amount of work performed by the engine (e.g.

kinetic energy production) is proportional to the temperature differential of the hot and cool reservoirs and the entropy change of a parcel through the cycle. The maximum theoretical efficiency is then given by

$$\varepsilon = (T_B - T_O)/ T_B. \quad (2.1)$$

where T_B and T_O are the temperatures of the boundary and outflow layers, respectively. This diagram also shows the effect of including the superintensity mechanism into E-MPI theory. Parcels that are able to penetrate into the low-level eye can access an additional reservoir of moist entropy. Eye parcels that are then returned to the eyewall cloud via mixing provide a 'turbo-boost' to the engine, akin to a second 'piston' for the TC engine.

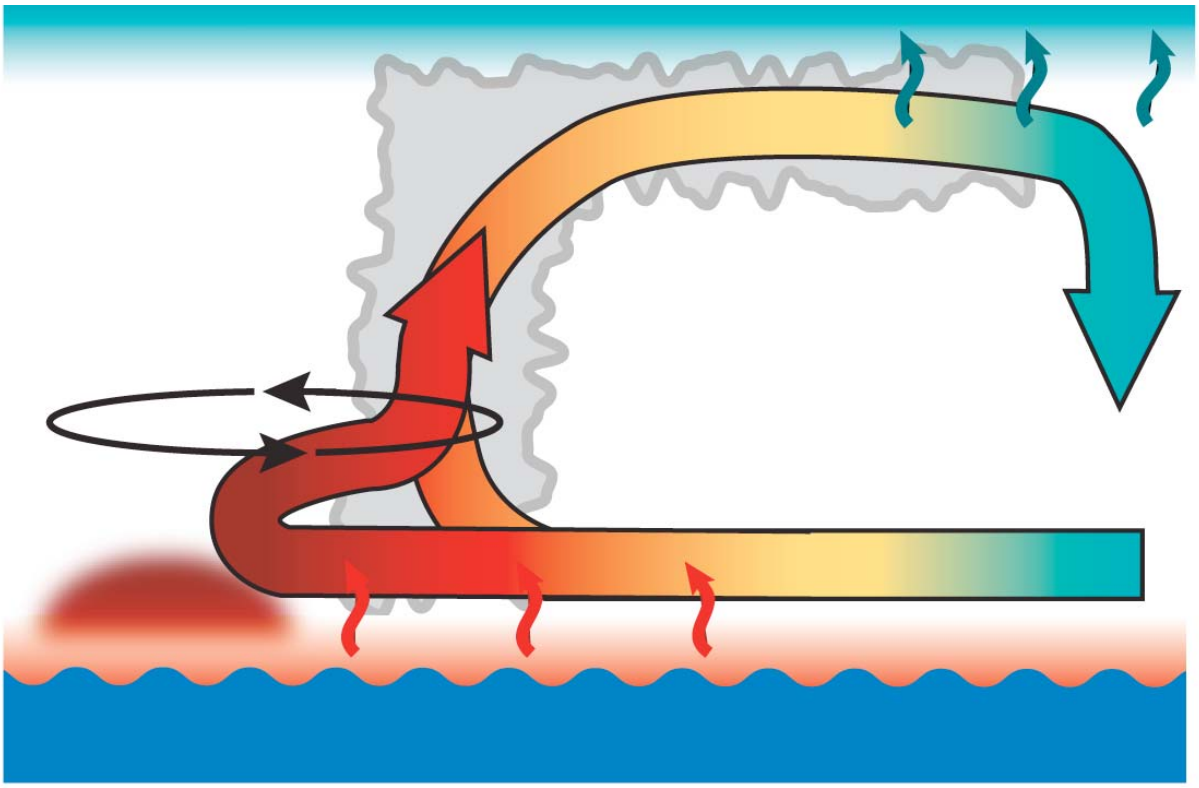

Figure 2.1: Idealized representation of the tropical cyclone Carnot engine, with the additional 'piston' provided by the superintensity mechanism.

The Carnot engine aspect of E-MPI is perhaps the most popular and simple concept of the theory, but it is the more rigorous mathematical derivation of the boundary layer energy balance that provides quantitative predictions for a given TC environment. The primary parameters that govern E-MPI are the sea surface temperature, the outflow temperature, boundary layer relative humidity, and the bulk enthalpy (Ck) and momentum (Cd) exchange coefficients. The exchange coefficients are the most uncertain of these predictors at wind speeds above category one, due to limited high-resolution surface flux measurements in the extreme conditions of a hurricane eyewall (Black et al. 2006). The other parameters can be measured by meteorological instrumentation in a particular TC's environment, yielding predictions for the maximum mean tangential wind at the top of the boundary layer. One purpose of this study was to test these predictions for an intense TC using high resolution in situ observations.

2.2 Tests of MPI

PM03 performed a rigorous test of E-MPI theory with the axisymmetric numerical model developed by Rotunno and Emanuel (1987), and found that the theoretical MPI was exceeded when the resolution of the model was able to more accurately simulate the hurricane eye. Their work suggested that the eye, traditionally passive in MPI theories, plays an important role in the thermomechanics of the TC engine by providing a reservoir of high moist entropy air that augments the energy available in the outer core and at the base of the eyewall. PM03 coined the term 'superintensity' to not only refer to storms which exceeded their MPI, but also in recognition of the thermodynamic mechanism by which this was achieved.

Comparable tests of MPI with observational data are limited. A climatological study of hurricane intensity by Tonkin et al. (2000) showed that both the Emanuel and Holland MPI theories demonstrated reasonable predictive capability for all ocean basins and seasons, with a general tendency for overestimation of the intensity. Given the wide range of adverse environmental conditions a tropical cyclone might encounter, this result is perhaps not too surprising. However, an interesting subset of storms that exceeded their MPI was also found. Figure 2.2, taken from their study, indicates a broad range of SSTs for which both MPI models underestimated the true TC intensity. Whether this is due to the use of climatological sea-surface temperature (SST) data, satellite-based intensity estimates, or a flawed theory is unknown. More detailed observations are clearly needed to elucidate the structure, intensity, and environmental parameters of the anomalous cases.

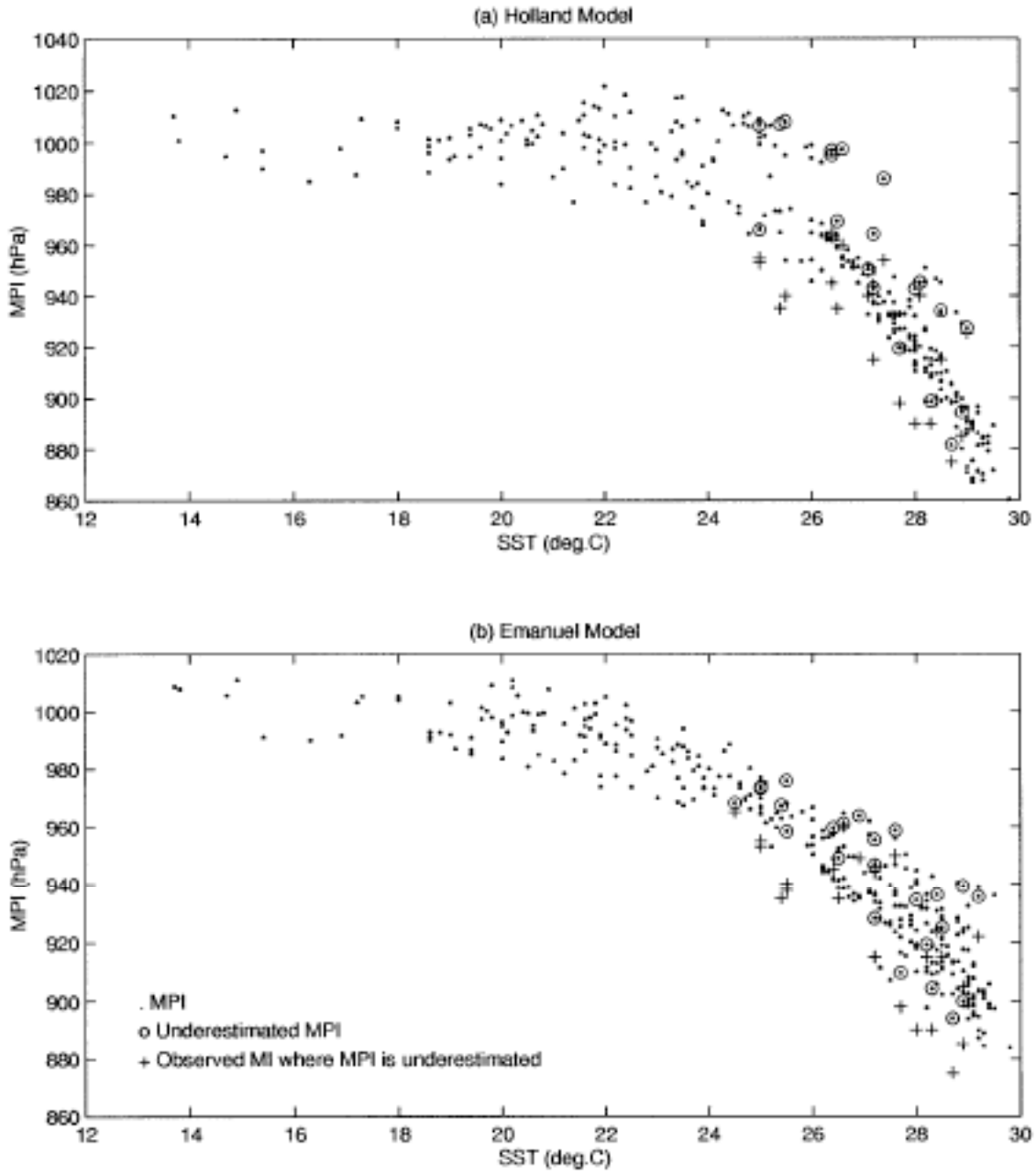

Figure 2.2: Holland and Emanuel MPI model estimates and the corresponding SST for (a) H-MPI and (b) E-MPI. model estimates. Model estimates that were noticeably underestimated (Circles) and the corresponding maximum observed tropical cyclone intensity (Plus signs) are also shown. [From Tonkin et al. (2000)]

Chapter 3

Dataset and analysis methodology

3.1 Hurricane Isabel (2003)

Hurricane Isabel became a tropical depression from an African easterly wave at 0000 UTC 6 September 2003, and was quickly named a tropical storm six hours later (Lawrence et al, 2005). This steady intensification continued until September 11th, when Isabel reached category five intensity on the Saffir-Simpson scale with estimated maximum sustained surface winds of 145 kts. Isabel maintained maximum sustained surface wind speeds above 130 kts and central pressures below 940 hPa in relatively favorable environmental conditions until September 15th, at which point vertical wind shear increased and the storm began to weaken. Isabel made landfall in North Carolina three days later as a large category two hurricane. The National Hurricane Center (NHC) best track and intensity are shown in Figure 3.1. The NOAA Hurricane Hunters conducted three IOPs from 12 – 14 September as part of the CBLAST and NOAA/NESDIS OCEAN WINDS experiments. National Hurricane Center (NHC) best track intensities were estimated at 140 kts during the ~16 – 23Z time period observations were collected on each day, making the storm a category five on the Saffir-Simpson scale during the IOPs.

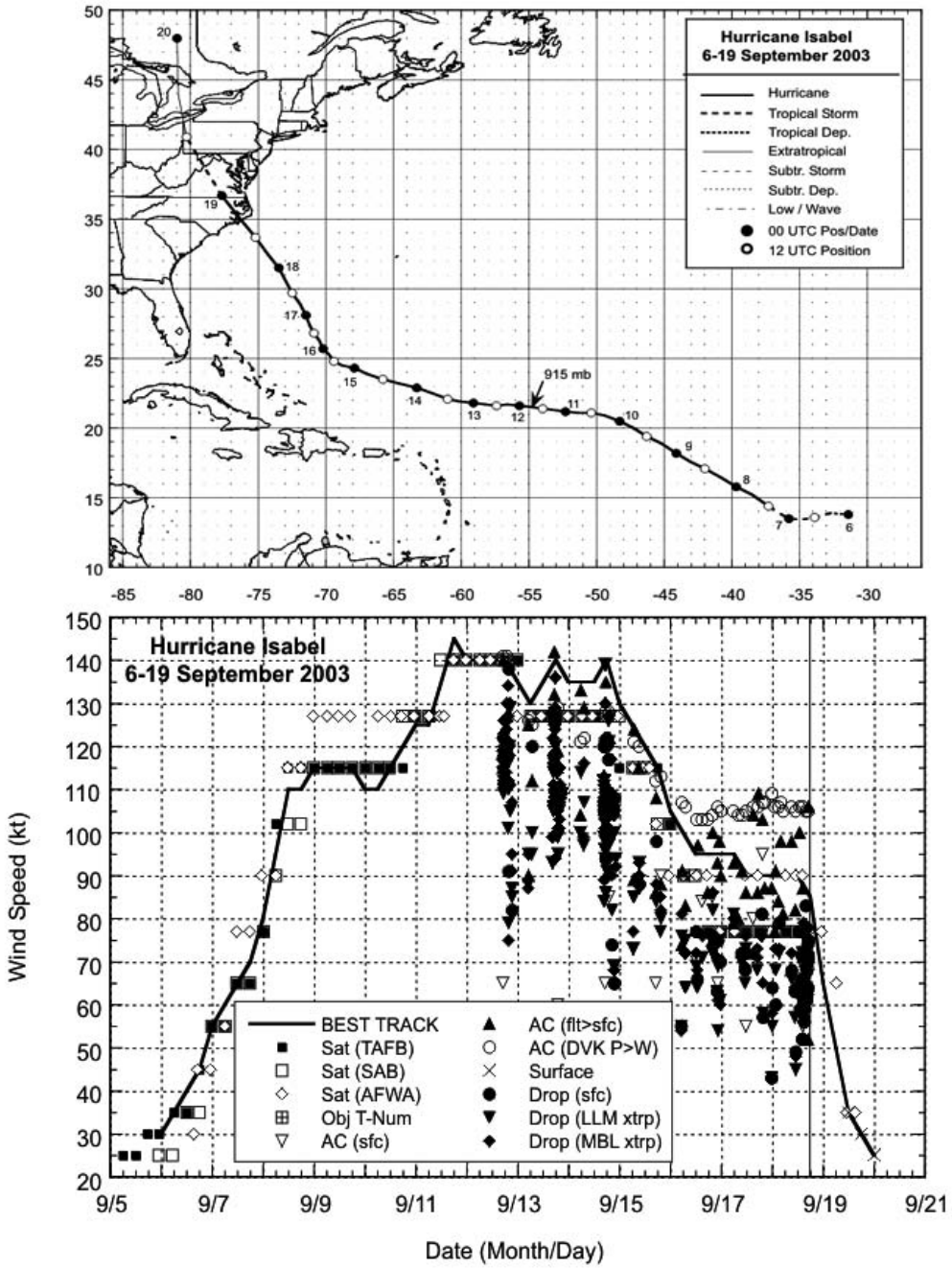

Figure 3.1 NOAA Tropical Prediction Center/National Hurricane Center best track for Hurricane Isabel. (a) Best track with minimum central pressure highlighted and (b) best track intensity. [From Beven and Cobb (2004)]

Two NOAA WP-3Ds (P3s), the NOAA G-IV, and United States Air Force (USAF) C130 aircraft collected in situ flight level and dropwindsonde data, with

additional Doppler radar and radiometer data obtained by the P3s only. This study focuses on the in situ, dropwindsonde, and radiometer data, but radar analysis was also performed for independent verification of the large-scale wind fields (not shown) and small-scale features (Aberson et al, 2006) presented in chapter 5. Equivalent potential temperature was calculated following the empirical formulation in Bolton (1980).

3.2 In situ Flight Level Data

Flight level in situ data used in this study was kindly provided by NOAA's Hurricane Research Division. Data was available at one second resolution for NOAA aircraft and ten second resolution for the Air Force C130s. A rudimentary correction for instrument wetting errors (Zipser et al. 1981; Eastin et al. 2002) was applied to supersaturated dewpoint temperature measurements. This correction assumes that the errors for the temperature and humidity sensors are equal in magnitude but opposite in sign, and was shown by Eastin et al. (2002) to reduce the majority of significant wetting errors but not remove them completely, resulting in a mean θ_e error of 2.7 K.

3.3 NCAR GPS Dropwindsondes

An unprecedented 184 National Center for Atmospheric Research (NCAR) Global Positioning System (GPS) dropwindsondes (sondes) were released into the inner and outer core of Hurricane Isabel during the three CBLAST IOPs. An additional 38 sondes were released in the ambient environment by the NOAA G-IV. This instrument provides pressure, temperature, relative humidity (PTH) and horizontal wind speed at 2 Hz temporal resolution along a Lagrangian trajectory falling at 12-15 m s^{-1} in the lower

troposphere. This yields a vertical resolution of approximately 5 m, with PTH typical errors less than 1.0 hPa, 0.2 C, and 5% respectively, and wind errors less than 2.0 m s^{-1} (Hock & Franklin, 1999). All dropwindsondes were quality-controlled (QCed) to remove noise and other instrument errors with either NCAR Aspen or HRD Editsonde software. For this study, all NOAA released sondes and most USAF sondes were kindly processed by HRD using Editsonde. Some USAF sondes were processed by the author using Aspen. Even though both of these programs are based the same QC algorithms, tests were performed to determine the differences, if any, between the two software packages.

A statistical comparison of the two processing packages was performed by Black (2005, personal communication) and found that the majority of sondes contained minimal differences after processing, but that there could be significant differences between the resulting profiles in some cases due to user choices, specific numerical implementation of the QC algorithm, or interpolation. Two fundamental differences between the two programs are that (1) Aspen does no interpolation between missing data points, whereas the Editsonde user has the option to fill in gaps where appropriate, resulting in a different number of data points in the post-processed data, and (2) Editsonde allows the user more freedom to manually interact with a particular sounding based on the user's experience and inspection of the individual data. A separate composite analysis for the 13th was therefore constructed using only Aspen processed dropwindsondes to determine the sensitivity to the processing scheme. Mean differences between this analysis and the present one were minimal with the exception of relative humidity and θ_e in the eyewall (see below), suggesting that no gross errors were introduced by the post-processing of the dropwindsonde data.

A more serious issue seems to have been the reporting of undersaturated measurements in the eyewall cloud by dropwindsondes released from the NOAA-43 (N43) P3. Recent analysis of humidity data in marine stratocumulus clouds by Wang (2005) suggests that newer (post-2002) dropwindsonde humidity sensors are not subject to an in-cloud dry bias like earlier models, due to the presence of a cap that protects the sensor prior to launch. If the cap is removed too early however, molecular contamination of the RH sensor can occur. Statistical analysis of the dropswindsonde humidity data showed that many of the sondes released from the N43 aircraft reached only ~85% RH in the eyewall. Since the theoretical value in precipitation and thick marine stratocumulus should be near 100%, this suggested a potential dry bias. However, the true homogeneity of the eyewall cloud is unknown, and arbitrary saturation of eyewall profiles was not justified. An RH correction is available as a user-selected option in Editsonde, but not in Aspen, that can be applied to dropwindsondes known to have fallen through saturated conditions (e.g. precipitation). This correction adds a scaled factor of the form

$$RH_{corr} = (100\% - Max\ RH) * (RH / Max\ RH) \qquad (3.1)$$

where RH_{corr} is the applied correction at a particular level, *RH* is the reported relative humidity at that level, and *Max RH* is the maximum value found anywhere in the sonde profile. This correction assumes that: (1) the dry bias is caused by molecular contamination of the sensor, not sensor failure, and therefore the variability in the reported RH captures true changes in the airmass, (2) the maximum value reported by the sonde should have been 100%, and (3) the bias is airmass dependent, i.e. moister values are skewed more than drier ones.

This correction was stable at ~12 – 15 % for the affected N43 dropwindsondes, suggesting that the degree of contamination was consistent for that batch of sondes. Though the applied correction seems plausible, the degree to which the corrected sonde profiles represent the true eyewall RH is still somewhat uncertain, however. To verify that the analysis was not overly sensitive to the uncertainty of these measurements, two additional composites were constructed without the suspect data and without applying any RH corrections (similar to that produced by Aspen post-processing). This led to a θ_e reduction in the eyewall of 2 - 4 K, comparable to the underestimate found for uncorrected instrument wetting errors. It is therefore believed that the post-processing of the relative humidity data removed all major errors, but potential sensor wetting and/or molecular contamination errors still yield an estimated θ_e uncertainty of ~3 K. While this uncertainty may have a distinct effect on the diagnosis of axisymmetric thermal wind balance (see section 6.2), it does not compromise the central conclusions of this study.

3.4 Vertical Velocity

Vertical velocity was obtained at flight levels from the measured wind near the aircraft, and was derived from the dropwindsondes by removing the estimated terminal fallspeed of the sondes as a function of pressure. This technique is shown to be relatively robust for mesoscale vertical motions in hurricanes (Franklin et al. 2003). For this study, the specific analytic formulation of fall velocity for the sonde detailed in the appendix of Hock & Franklin (1999) was reduced to a simpler linear formula for the lower troposphere given by $dz/dt = 22 - p*(10^{-5} ms^{-1}Pa^{-1})$, which is approximately equivalent up to ~600 hPa. The theoretical fall speed is shown in Figure 3.2. Given

uncertainties of the drag coefficient and parachute response of the dropwindsonde in the extreme wind speeds of Isabel's eyewall, this approximation is believed to be on the order of the estimated error of 0.5 – 1.0 m s^{-1} in vertical wind measurement.

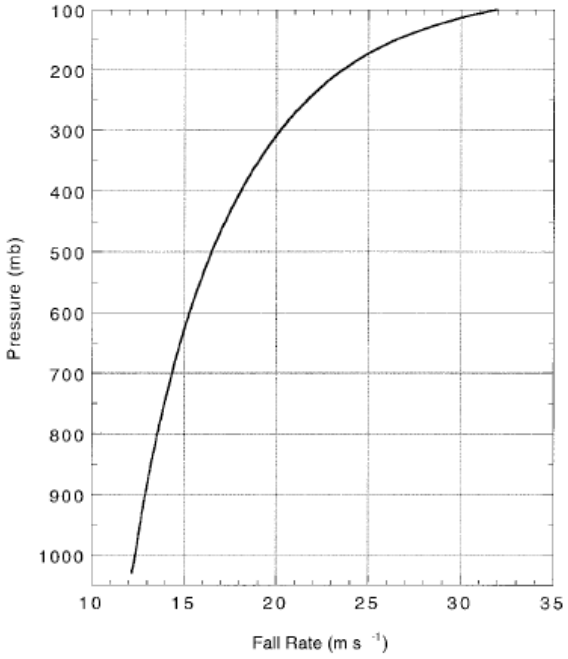

Figure 3.2: Theoretical fall velocity of the dropwindsonde as a function of pressure. [From Hock and Franklin 1999]

3.5 Diagnosed TC centers

It has long been recognized that meaningful analysis of vortex structure can be obtained by viewing observations in a storm-relative cylindrical coordinate system. Cylindrical coordinates allow for the representation of the windfield by tangential and radial components, and structural decomposition into azimuthal harmonics (wavenumbers). The resulting axisymmetric (wavenumber zero) storm structure is more robust to center uncertainty than its asymmetric counterpart (Lee and Marks 2000), but still requires accurate center estimates for a proper coodinate transformation.

The center-finding method of Willoughby and Chelmow (1982, hereafter WC82) relies on both pressure and wind information from high-resolution flight level data, and has been shown to be accurate to ~3 km. WC82 shows that a dynamic center, defined as the nondivergent streamfunction minimum, must exist for a closed vortex. As the aircraft approaches the closest point of approach (CPA) to this dynamic center, the 'Willoughby function' H given by

$$H = V^2 + gD \tag{3.2}$$

where V is the tangential velocity, g the gravitational acceleration, and D is the departure of a selected isobaric height from its value in the standard atmosphere, reaches a minimum. A window of 50 seconds before and after the CPA is then defined, and lines are drawn normal to the wind direction at each second. This is illustrated in Figure 3.3, showing the clustering of the intersection of the lines of position (LOPs) near the TC center. In an axisymmetric vortex, the lines would converge to a point. In a real hurricane, each LOP has a separation from the true center defined by s_n. The weighted root mean square (RMS) of the separation is then given by

$$S_L^2 = (\sum W_n)^{-1} \sum W_n s_n^2 \tag{3.3}$$

where W_n is a weighting factor set to 10 when s_n is the determined from the CPA, and 1 for all other LOPs in the window. Minimizing S_L^2 yields the center fix for that time period. Storm relative centers are obtained by subtracting the storm motion vector from the winds in the CPA window and then minimizing S_L^2.

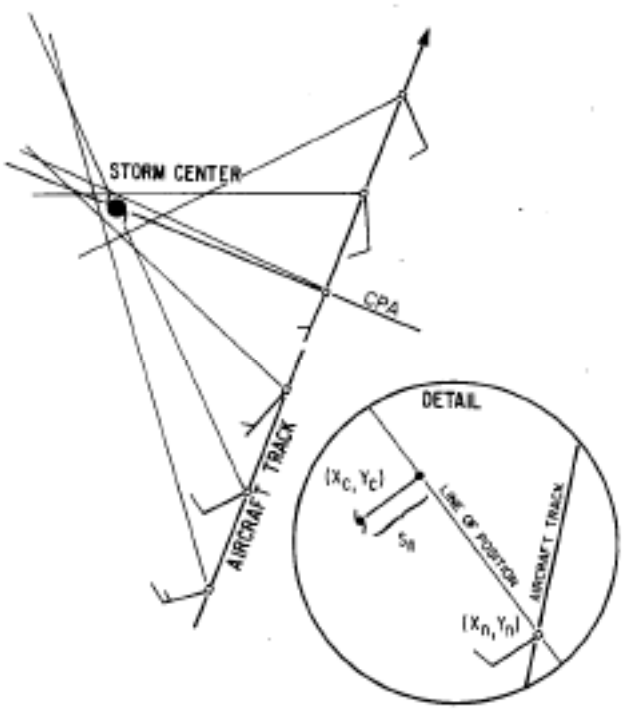

Figure 3.3: The geometric relationship between the aircraft track, closest point of approach (CPA), lines of position (LOPs), and dynamic center. [From Willoughby and Chelmow 1982]

The variable time interval between fixes, variability of the center with height, and local pressure and wind minima associated with meosvortices in the eye makes determining an accurate set of centers for an entire IOP challenging. The analyzed set of centers for each day was created by a linear interpolation between selected robust center fixes obtained by the WC82 method using storm-relative winds at 2 km height, with constraints provided by NHC best track data when reliable center fixes were not available. This yielded a general west-northwesterly storm motion of ~ 7 m s^{-1} on each day.

Errors in the analysis introduced by center uncertainty were then examined by perturbing the estimated center on the 13th in a random direction up to 5 and 10 km for every observation. This has the effect of changing the relative location of each

measurement without regard to the specific time it was collected, and accounts for center uncertainties resulting from small-scale oscillations, interpolation error, and vortex tilt. This sensitivity test yielded RMS differences in the composite tangential and radial wind velocities of 1.3 (4.1) and 0.76 (1.9) m s^{-1}, respectively for the 5 (10) km perturbations. Scalar quantities had very low RMS differences. Dropwindsondes released in the eye were examined individually for center errors, due to the increased sensitivity of the cylindrical coordinate transform at small radii. Given the accuracy of the individual center fixes and relative robustness of axisymmetric quantities, there appear to be no systematic errors introduced by an estimated ~5 km mean center uncertainty.

3.6 Barnes Objective Analysis

After quality control and decomposition into storm-relative cylindrical coordinates, the resulting data distribution in the radial-azimuthal and radial-vertical planes for each IOP is shown in Figure 3.4. There is excellent azimuthal coverage on each day, with some limited data gaps in the lowest levels between the eye and eyewall on the 13th and 14th. The irregular, dense distribution in the radial-vertical plane suggested compositing using Barnes objective analysis (Barnes 1968, Koch et al. 1983) to obtain the axisymmetric structure. This analysis requires several assumptions: (1) Isabel was axisymmetric, (2) steady state, and (3) the observations from the different platforms and instruments were similar in scale. Given Isabel's generally annular appearance as observed by satellite (Figure 3.5, left column) and the impressive azimuthal sampling of the storm, the assumption of axisymmetry in this analysis is well satisfied on all three days. Isabel's asymmetric structure, evident in the dramatic low-

level stratus cloud structures in the eye in Figure 3.5 (right column), was critical to her maintenance and evolution, but is typically an order of magnitude smaller than the primary circulation in the eyewall. Limited observations in the low-level eye preclude a meaningful separation of the kinematics and thermodynamics into azimuthal mean (vortex) and asymmetric (eddy) components in that region. However, the resulting fields yield approximate representations of the eye structure and clearly show evidence of evolution over the three analysis days. Though the composites show distinct structural evolution of the TC, the satellite appearance and maintenance of category five intensity suggest that the storm was evolving slowly during this time period and was therefore nearly steady state during the 7 hours of each IOP. The resulting best track from this period is consistent with this assumption.

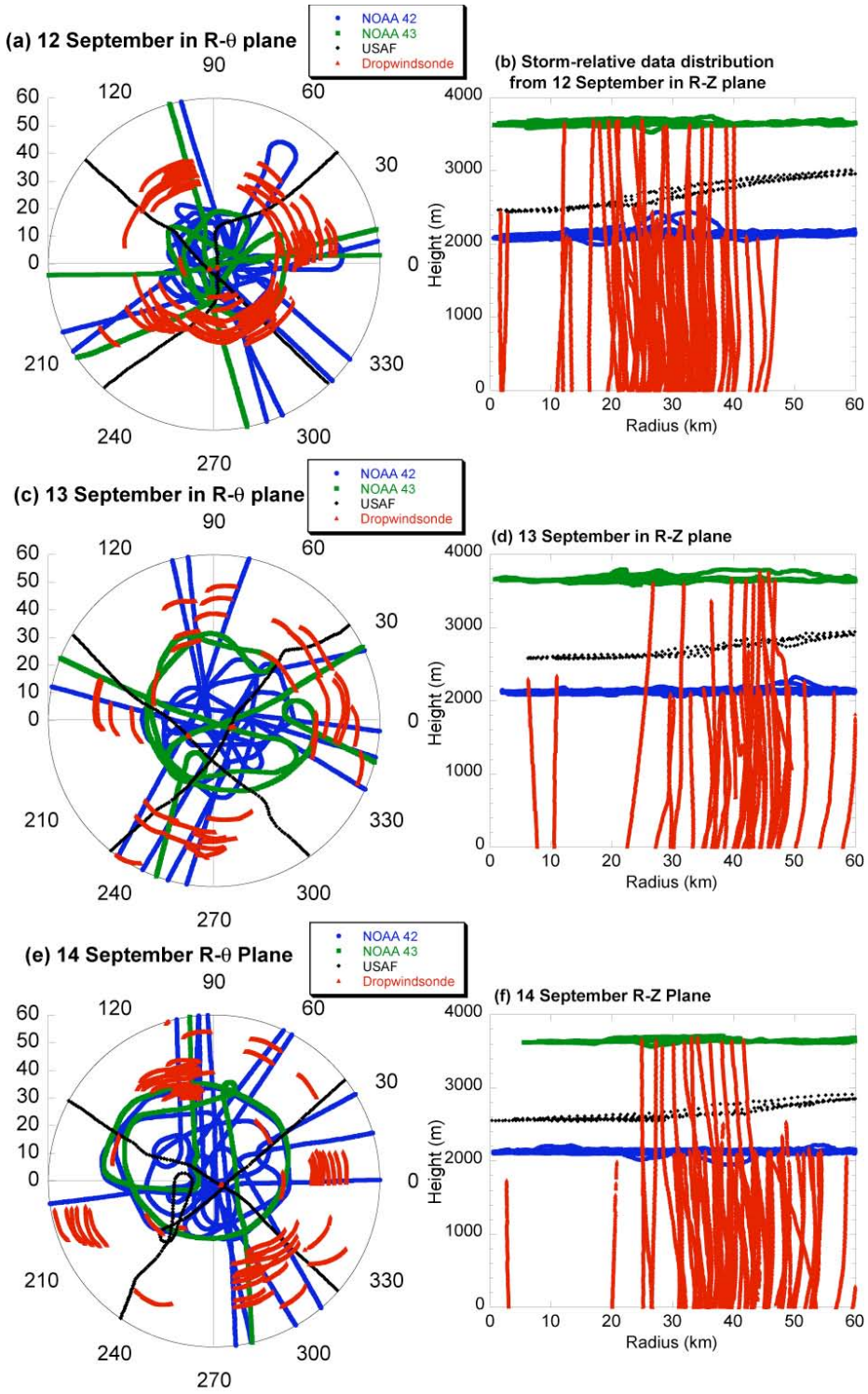

Figure 3.4: Dropwindsonde locations and trajectories and aircraft flight tracks relative to storm center from 16 – 23 UTC on each day. Storm-relative data distribution in the (left) azimuthal (R-θ) plane; and (right) radial-height (R-Z) plane, showing the NOAA P-3 (42 in blue, 43 in green), USAF C-130 (in black) flight tracks, and dropwindsonde

trajectories (in red). The dropwindsondes in the left column move cyclonically (counterclockwise).

Figure 3.5: Satellite appearance of Hurricane Isabel at 85 GHz (left, courtesy NRL/Monterey) and visible (right, courtesy CIRA/CSU) wavelengths during each IOP.

85 GHz brightness temperatures are from (a) TMI at 12/2126 UTC, (c) SSMI at 13/2218, and (e) TMI at 14/2110. Visible images are from GOES super-rapid-scan operations 1745 UTC on each day.

Combining flight level and dropwindsonde data requires an examination of the type of measurements taken by these observing platforms. The flight level data can be considered primarily Eulerian in that the aircraft motion is relatively independent of the storm circulation. However, these measurements are still being taken at 1 Hz from a platform moving at ~100 m s-1 through the flow, yielding an implied horizontal spatial range of ~100 m with a few meters of vertical extent depending on turbulence and deliberate altitude changes. The dropwindsonde data on the other hand is primarily Lagrangian, falling through the storm circulation at ~12 m s-1 and being carried along with the flow horizontally at speeds up to 107 m s-1. Measuring at 2 Hz implies a vertical resolution of ~5 m, with a variable horizontal resolution of up to 50 m. By making the steady state, axisymmetric assumption, these two types of measurements can both be treated as axisymmetric, instantaneous snapshots in the radial-vertical plane of the storm circulation with variable spatial resolution. The reported GPS position of the aircraft or dropwindsonde measurement is then weighted according to its distance from a given storm relative radius and altitude (gridpoint). The weighted observations from different azimuths and times are then averaged by the Barnes analysis to yield an estimate of the axisymmetric structure at a coarser spatial resolution than that implied by the individual measurements.

A total of ~43500, 30700, and 37800 datapoints were available on each day from dropwindsonde and flight level data. The sounding data comprised 63 %, 48%, and 59% of the data distributions for each IOP, from 67, 35, and 58 inner-core (< 60 km radius)

soundings, respectively. The Barnes analysis procedure used radial and vertical grids of 2500 m and 250 m, respectively, to account for the relatively shallow nature of the hurricane and respective data distribution. A minimal gamma 'smoothing' parameter of 0.3 and radial and vertical weight parameters were then set to produce the maximum spectral resolution (10 km and 1 km, respectively) allowable for the given grid spacing. Higher resolution grids than this tended to produce discontinuities in the data poor regions. These scales are believed to accurately capture the fundamental structure governing the hurricane intensity, however.

The composite transverse circulation presented here therefore does not necessarily satisfy the axisymmetric mass continuity equation at every grid point. Uncertainties arising from under-sampling, the location of the circulation center, and dropwindsonde terminal fall speed may produce unbalanced divergence and vertical velocity fields at any particular point, resulting in a non-zero residual in the mass continuity equation. Given the relatively high spatial resolution of the composite, radial and vertical derivatives were calculated from the gridded values in an attempt to quantitatively describe this residual. Unfortunately, the resulting *dw/dz* calculation was too sensitive to accurately determine the degree to which the analysis satisfied the mass continuity equation.

Calculation of gradients from observed data is often problematic due to interpolation and missing data. Given the relatively dense observations however, an attempt was made to assess kinematic and thermodynamic gradients derived from the composite in the inner core. Gradients of the horizontal winds calculated from the composite were the most robust, based on comparison of scatterplots (not shown) and binned averages of the raw data versus the composited fields. Derivatives of other

quantities were in many cases too noisy to draw any reliable quantitative conclusions, and appeared to underestimate the gradients in many cases. The divergence, vorticity, and potential vorticity (which also involves the potential temperature gradient) resulting from these calculations are therefore presented in chapter 4, with the caveat that some of the fine-scale structure and exact magnitude may be grid dependent. For sensitive calculations, such as those involving the pressure and θ_e in the balance equations, obtaining the gradient magnitude was the primary objective, and derivatives were calculated from radially and vertically binned averages instead of the composite data. This technique is believed to more accurately capture the magnitude of the gradients at a particular vertical level, with the cost of decreased radial spatial resolution.

Chapter 4

Axisymmetric Structure and Evolution from 12 – 14 September

4.1 Axisymmetric Composites

This analysis of Hurricane Isabel suggests that despite the relatively steady state intensity, the storm slowly evolved structurally from 12 – 14 September. Figure 4.1 shows the radius-height composite storm-relative tangential wind (color), radial wind (contour), and secondary circulation (vector) in ms^{-1}. The origin (0, 0) denotes the storm center at the ocean surface. The core region of maximum tangential winds decays from ~80 m s^{-1} to 74 m s^{-1}, but also rises from ~500 m to 1 km altitude and expands from an RMW of ~25 km to 45 km. This wind, by virtue of the averaging required to compute it, is likely comparable to a sustained wind. The observed sharp tangential wind gradient along the inner edge of the eyewall is consistent with the presence of local Kelvin-Helmholtz instabilities and associated lateral mixing across the eyewall interface (e.g., Schubert et al. 1999; Montgomery et al. 2002). An extreme wind speed maximum (107 ms^{-1}), which would likely have been experienced by an anemometer as a gust, was observed by a dropwindsonde near 30 km radius at 1.4 km altitude on the 13th (see chapter 5 and Aberson et al. 2006, for details). Near this region, tangential velocity measurements were highly variable azimuthally, consistent with the presence of mesovortices in the eye-eyewall interface.

Figure 4.1: Radius-height azimuthal mean storm-relative tangential wind (color), radial wind (contour), and the secondary circulation (vector) in ms^{-1} derived from GPS dropwindsonde and flight level data from 12 - 14 (a – c) of September, 2003.

The low-level radial flow increased in both depth and intensity from the 12th to the 13th, but then weakened again on the 14th. A persistent region of ~5 - 10 m s-1 outflow just above the boundary layer is evident on all three days. The derived vertical velocity is qualitatively consistent with the radial divergence, showing weak vertical motions inside the eye and a maximum updraft nearly co-located with the RMW on each day. Lowest-level (0-250 m) radial inflow of 20 ms^{-1} located 25 km radius from the center suggests significant penetration of air from the eyewall into the eye on the 13th. Since only a single sounding was available in this region during this IOP, sensitivity of the radial wind to the center placement was tested to verify this feature (Fig 4.2). All reasonable center estimates yield varying degrees of inflow and an approximate radial location near ~25 km. This radial location is well within the pentagonal shaped eye at this time according to the radar reflectivity (Fig 4.3). The Air Force fix from this time, which includes pressure information (like WC82) and visual evidence, gives very consistent kinematics with the N42 storm-relative center and is estimated to an accuracy of less than 8 km. This intense inflow measurement appears to be robust, but may be associated with a mesovortex and not necessarily be representative of the axisymmetric inflow at this radius.

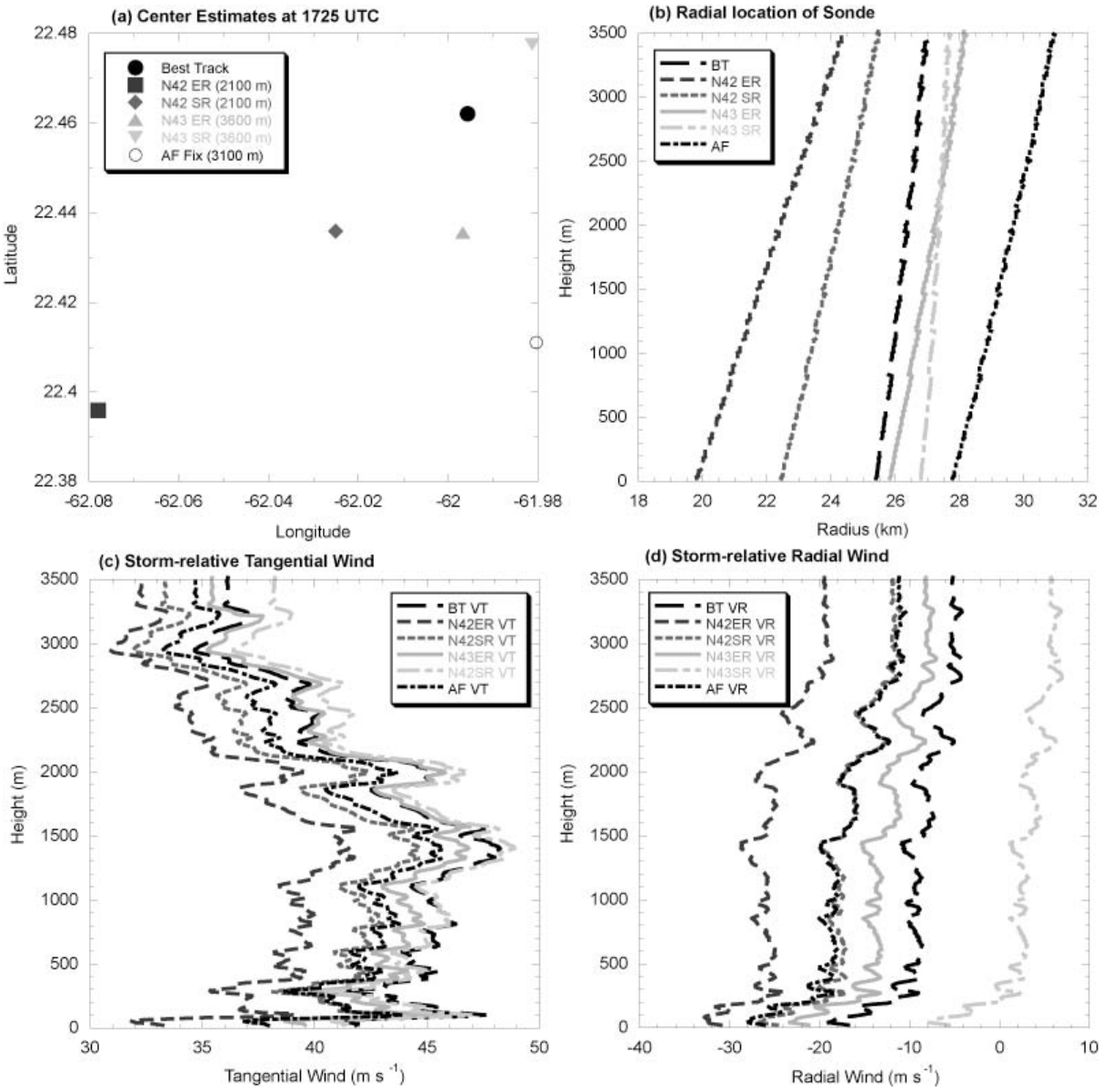

Figure 4.2: The uncertainty in the storm-relative winds for sonde g022615278 using different centers (BT = best track, AF = Air Force Fix, N42(43) SR(ER) = NOAA 42 (43) using storm (earth) relative winds with the WC82 method). N42SR centers comprise the set used in this study, yielding a radius of ~24 km and average inflow of ~20 m/s. Other center estimates are within the 10km x 10km box, and all yield inflow of varying degrees.

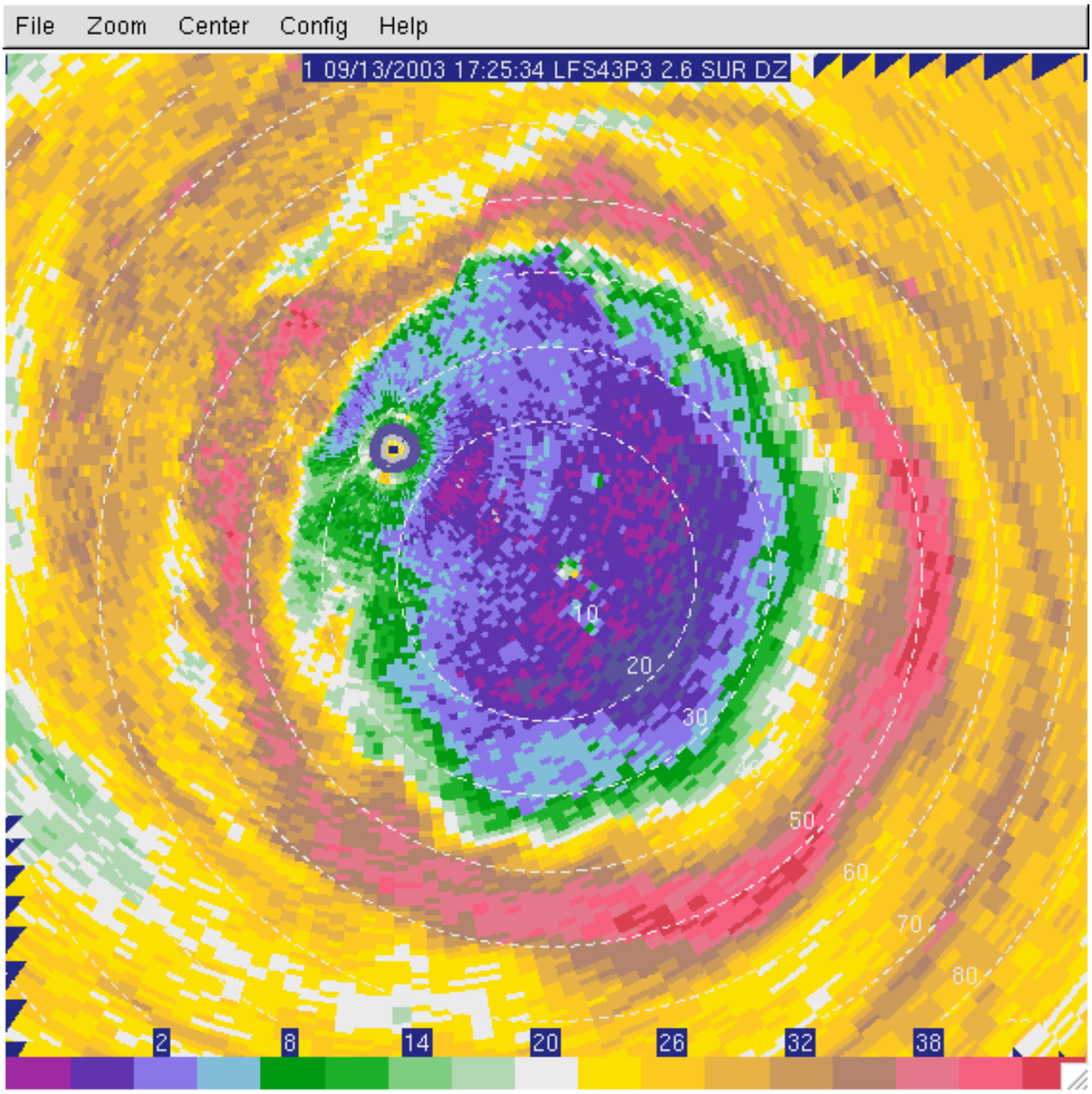

Figure 4.3: Pentagonal eyewall reflectivity structure as seen from NOAA 43 lower fuselage 5 cm radar at 1725 UTC. Small circle in northwest corner of eye is aircraft location and sonde release point.

Figure 4.4 shows the radius-height composite equivalent potential temperature (θ_e – in color), specific absolute vertical angular momentum (contour), and transverse secondary circulation (vector). The specific absolute vertical angular momentum

(absolute circulation) is $M = rv + \frac{1}{2} fr^2$, where r is the radius from the vortex center, v is the storm-relative tangential wind, and f is the Coriolis parameter. Some of the most dramatic changes in storm structure are illustrated here, with a distinct increase in low-level theta-e in the eye from the 12th to the 13th, followed by an increase in mean eyewall theta-e on the 14th. The radial theta-e gradient is generally negative throughout all three days, except for very near the center on the 12th. Indications that θe was beginning to build on this day are evident however, with a shallow local surface maxima at ~10 km radius of 373 K where the wind speed was somewhat higher (not shown).

By the IOP on the 13th, the dropwindsondes and in situ data inside of 30 km had consistently higher theta-e values, suggesting that a significant amount of high moist entropy air was then present in the low-level eye. The analysis (Figure 4.4b) suggests that the high entropy air returns in the outflow above 1 km, as indicated by the outward bulge in the θ_e contours above 1 km altitude. The small outward bulge evident in the analyzed absolute angular momentum near 37 km radius and 2 km altitude provides additional evidence of this exchange, consistent with the injection of this high θ_e air into the eyewall. On the 14th, it appears as if the θ_e has been 'mixed out', with relatively lower theta-e values and gradients found in the eye, and an increase in the mean theta-e at the eyewall. While this analysis does not preclude the idea of asymmetric, isolated pockets of high theta-e in the eye aliased onto the mean, these figures suggest that there were significant changes in the mean moist entropy structure over these three days. The increase in θ_e after the 12th occurred despite a rise in central pressure of ~10 hPa, and appears to be primarily due to increased low-level relative humidity. This supports the idea of persistent latent heat flux in the low-level eye, and possibly radial moisture flux

due to mixing from the eyewall. Though a detailed calculation of the residence time of air parcels in the eye is beyond the scope of this study, the apparent increase to near saturation θ_e* (~376 K) suggests that a significant portion of parcels remained in the eye and moistened over this period. Cram et al. (2006) showed in their numerical simulation of Hurricane Bonnie that residence times for significant θ_e gain were commonly on the order of 40 – 60 minutes, however.

The concurrent increase of the moist entropy, vertical velocity, and radial inflow from the 12th to the 13th suggests a positive feedback between these fields. The addition of higher θ_e to the eyewall cloud enhances (locally) buoyant updrafts (Eastin et al. 2005), which in turn drives a stronger radial inflow by mass continuity. This increased inflow may enable more parcels to penetrate the eyewall and access the moist entropy reservoir in the eye. The increase in radial inflow was also associated with an increase in angular momentum, suggesting that this higher momentum air was advected inward from the outer core. There is some evidence that the expansion of the RMW was possibly due to an eyewall replacement cycle over this period. Reflectivity analysis (not shown) suggests a consolidation of an outer rainband on the 12th, but the lack of a clear secondary wind maximum and failure of the outer eyewall to contract provide inconclusive evidence of an eyewall replacement.

Figure 4.4: Radius-height azimuthal mean storm-relative θ_e (color, in Kelvin); absolute angular momentum (contour, $m^2s^{-1}\times10^6$); and transverse secondary circulation (vector) from 12 – 14 (a –c) of September, 2003.

Figure 4.5: Radius-height azimuthal mean storm-relative Rossby-Ertel potential vorticity (color, in PVU), and absolute vertical vorticity (contour, in s-1*10-3) from 12 – 14 (a – c) of September, 2003.

As Isabel crossed the cool wake of Fabian on the 13th, one might expect the intensity to have decreased significantly, but this analysis indicates otherwise. In fact, one sees only a slight decrease in the (potential) vorticity of the vortex each day, as shown in Figure 4.5, due to a continuing expansion of the windfield and weakening of the radial gradient of tangential wind. The mean peak tangential wind at the RMW remained above 74 m s^{-1}, however. The composite vorticity is generally positive everywhere in the domain, with the exception of a small area near 10 km radius on the 14th. This is believed to be an artifact of the analysis resulting from the lack of data and weak radial gradient of tangential wind in this region. For consistency with the other plots, these datapoints were left in the final analysis despite the suspect values since the remaining potential vorticity structure seemed reliable.

The axisymmetric Rossby-Ertel PV was calculated from the composite gradients of axisymmetric tangential velocity and potential temperature in cylindrical coordinates by

$$\alpha\vec{\zeta}\cdot\nabla\theta = \alpha\left(\left(f+\frac{\partial(rv)}{r\partial r}\right)\frac{\partial\theta}{\partial z}-\frac{\partial v}{\partial z}\frac{\partial\theta}{\partial r}\right) \tag{4.1}$$

where α is the specific volume, ζ the vorticity vector, v the tangential wind, and θ the potential temperature. The 'hollow tower' or ring structure of PV at ~1 km altitude is clearly evident on all three days (Figure 4.5), suggesting that the vortex meets the requirements for barotropic instability. The appearance of a pentagon of high reflectivity from a NOAA P3 lower fuselage radar image at approximately the same time (Figure 4.3), in conjunction with GOES super rapid scan animations (not shown), corroborate the existence of coherent mesovortices in the vicinity of the eyewall that have been predicted by high resolution numerical simulations (Schubert et al. 1999; Kossin and Schubert

2001; Persing and Montgomery 2003; Kossin and Schubert 2004) and liquid-water laboratory experiments (Montgomery et al. 2002). The mesovortices are believed the result of a combined barotropic/baroclinic instability associated with the annulus of potential vorticity near and within the eyewall cloud; the potential vorticity annulus is generated by latent heating and vortex tube stretching in the eyewall (Schubert et al. 1999; Nolan and Montgomery 2002).

While providing localized extreme winds, eyewall mesovortices in the lower troposphere are also thought to play an important role in the storm's dynamics and energetics. In barotropic and baroclinic vortex models that neglect diabatic processes and/or the secondary circulation, the instability causes a breakdown of the eyewall into small-scale mesovortices, weakening the storm-scale azimuthal tangential wind field (Schubert et al. 1999; Kossin and Schubert 2001).

In conjunction with a secondary circulation driven by latent heating, surface friction and eddy processes, however, eyewall breakdown in the lower troposphere permits inflowing air parcels to penetrate the otherwise highly impermeable eyewall region (e.g., Shapiro 1983, Sec. 2; Emanuel 1997, Sec, 3; cf. Rotunno 1984). Inflowing parcels that reach the low-level eye and spend some time inside it can increase their moist entropy through interaction with the ocean. The combined effect of the near-surface mean inflow/outflow circulation and mesovortices is to transport and stir high entropy air from the low-level eye to the eyewall (Schubert et al. 1999; Braun 2002; Persing and Montgomery 2003; Braun et al. 2005; Cram et al. 2005; Eastin et al. 2005). In this way, the thermodynamic energy drawn from the underlying ocean within the eye provides additional power to the hurricane engine relative to that obtained from the ocean underneath and outside the

eyewall where current theory assumes all of the energy uptake occurs (e.g., Emanuel 1997). The in-situ observations analyzed here suggest that this thermodynamic boost exceeds the weakening tendency associated with the breakdown of the eyewall.

The double maxima of PV are associated with the strong radial shear (outer) and eye thermal inversion (inner, upper), respectively. The eye maximum at ~3 km altitude corresponds well to a transition region with a sharp decrease in relative humidity values (not shown), and weak subsidence/near-zero vertical velocity. While some of the fine-scale detail and exact magnitude of the PV fields is most likely due to the particular data sampling and compositing technique, the consistent structure on all three days provides confidence that the gross features of this important dynamical quantity are captured effectively by this analysis. This structure is also qualitatively consistent with numerical modeling results (Wang and Zhang, 2003), which show a similar feature in the low-level eye of Hurricane Andrew (1992) at ~2.5 km altitude, and the bowl-shaped maximum just inside the RMW typically associated with very intense vortices (Figure 4.6). The dynamical role of the PV maximum in the low-level eye is an interesting question for future research.

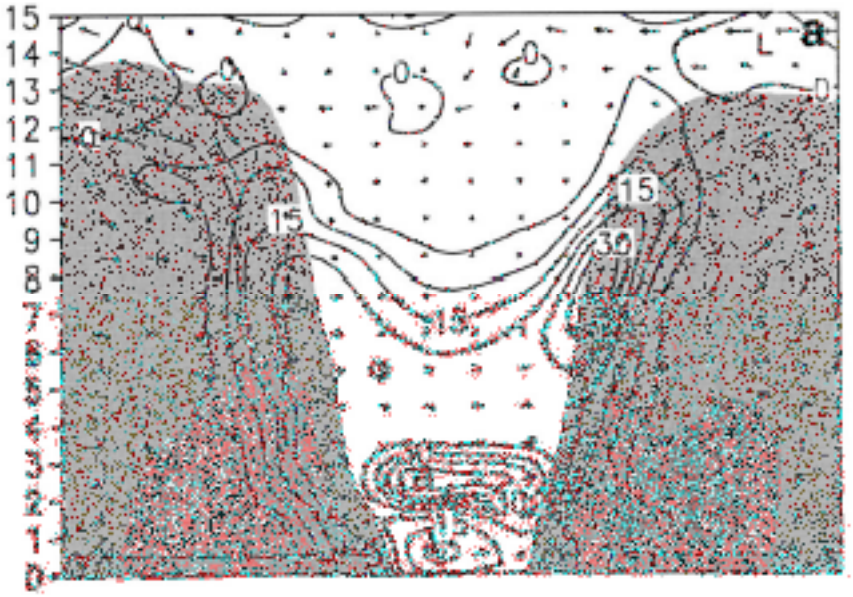

Figure 4.6: West–east vertical cross sections of PV (contoured), superposed with storm-relative in-plane flow vectors, from the model output (every 5 PVU). They are obtained by averaging 15 datasets at 4-min intervals during the 1-h period ending at 2100 UTC 23 Aug 1992. Shadings denote the simulated radar reflectivity greater than 15 and 35 dB*Z*, which represents roughly the distribution of precipitation with two different intensities. Solid (dashed) lines are for positive (negative) values. Note that vertical velocity vectors have been amplified by a factor of 5. [From Wang and Zhang (2003)]

The PV presented here is the traditional "dry" Rossy-Ertel PV, calculated by the inner product of the absolute vorticity vector and gradient of potential temperature. It is important to note however, that part of the simplicity of the E-MPI framework arises through an assumption of zero "moist saturated" PV, in which the potential temperature is replaced by saturated equivalent potential temperature (θ_e*) in Equation (4.1). In a zero θ_e*-PV vortex, lines of constant absolute angular momentum and saturated moist entropy are congruent above the boundary layer, allowing for a PV through knowledge of the boundary conditions alone. Thus, the complete balanced wind and thermal fields can be obtained through knowledge of the radial structure of θ_e in the boundary and outflow layers, and assumption of saturation throughout the free troposphere. This analysis

suggests that while the M and θ_e lines are indeed nearly parallel throughout much of the inner core, there are significant deviations from zero θ_e-PV, even in the saturated eyewall, on all three days. This is consistent with radial mixing of θ_e, local buoyancy enhancement in the eyewall, and the superintensity mechanism.

The 'correct' thermodynamic variable used to construct PV maps is debatable. Recent work by Schubert (2004) confirms that θ_e*-PV is invertible, but point out that it does not have the correct limiting case in areas where the RH falls below 100%. θ_e by itself is not invertible, but approaches Rossby-Ertel PV in the dry limit. Schubert suggests a different definition of moist invertible PV using θ_ρ, which is dynamically similar to Rossby-Ertel PV but includes the total moisture density of vapor, cloud water, and precipitation. Exploration of the differences between these different potential vorticity concepts using observational data is a topic for future work.

4.2 Radial structure of Boundary Layer θ_e and Humidity

A key to understanding the intensity problem is the amount of moist entropy a parcel is able to gain in the TC boundary layer. MR60 posited that almost all of the entropy gain occurs on the inward spiral from the environment to the eyewall. Conversely, Emanuel (1986) argued that convective downdrafts in the rainbands prevent significant material change of moist entropy in the outer core, and that most of the increase occurs directly under the eyewall. PM03 explored a third mechanism, in which strong enthalpy fluxes in the low-level eye provide an important additional source of moist entropy for the hurricane engine. Boundary layer mean soundings with 50 m

vertical resolution were therefore constructed to determine the relative character of air parcels at different radii from the storm center.

Different colors and line styles are used in Figure 4.7 to denote the respective soundings from the eye (0 – 15 km radius, red), nominal eyewall (20 – 30 km on the 12th, 40 – 50 km radius on the 13th and 14th , orange), outer core (~200 km radius, green), and ambient environment (300 – 1000 km radius, blue) and date from 12 (solid), 13 (long dash), and 14 (dotted) of September. Notably, the outer core values of all quantities were similar for each IOP. This indicates that the gain in θe for parcels spiraling into the eyewall was the largest on the 12th (~11 K) and smallest on the 13th (~4 K). An additional ~4 K and ~14 K, respectively was available for parcels that were able to access the eye however. Given that the tangential velocity remained nearly steady state, implying that the frictional dissipation was similar on each day, the required moist entropy to maintain the intensity on the 13th thus most likely originated in the eye. It is also interesting to note that the inner-core SST was the lowest on this day (~27.5 C), suggesting that the reduced latent heat fluxes at the eyewall were compensated for by radial fluxes from the eye. Isabel appears to have settled into an intermediate structure on the 14th, with an ~6 K increase from the outer core and an additional ~7 K into the eye. This analysis suggests that a total of 13 – 18 K of moist entropy gain was possible for a inflowing parcel on all three days via differing thermodynamic pathways.

Relative humidity in the outer core and eyewall is nearly the same on each day (Figure 4.7b), but the eye soundings are remarkably different. Only the 13th shows a deep moist layer extending above 2 km, but the 12th and 14th have only a shallow (~1 km) deep

moist layer with the humidity dropping off rapidly above that. This is the primary reason that the highest θe values are found in the eye on the 13th.

Figure 4.7: Boundary layer θ^e, and relative humidity from 12 – 14 September. Colors represent the different radial bins of the eye (0 – 15 km radius, red), nominal eyewall (20 – 30 km on the 12th, 40 – 50 km radius on the 13th and 14th , orange), outer core (~200 km radius, green), and ambient environment (300 – 1000 km radius, blue). Line styles indicate the sounding date from 12 (solid), 13 (long dash), and 14 (dotted) of September.

Chapter 5

Asymmetric Structure and Extreme Wind Speeds

The preceding analysis precludes discussion of asymmetric features due to heavy spatial and temporal averaging. As mentioned previously however, the asymmetric storm structure likely plays an important role in TC intensity changes. Additionally, small scale features and a wavenumber one asymmetry resulting from vortex translation are extremely important in producing severe ground-relative winds and hurricane damage. This chapter provides a brief analysis of one quadrant of the storm on the 13th where the strongest known horizontal wind was directly measured in a tropical cyclone (TC). Much of this discussion is largely taken verbatim from Aberson et al. (2006), where a more detailed analysis of this extreme wind measurement is presented. Relevant sections, including the Doppler radar analysis performed as part of this thesis research, are presented here for completeness.

At 1752 UTC 13 September 2003 a GPS dropwindsonde (Hock and Franklin 1999) was released just inside the eastern edge of the eyewall of Hurricane Isabel just below 750 hPa, or about 2 km above mean sea level. The dropwindsonde encountered a very strong updraft and horizontal wind at the top of a saturated air layer (Figure 5.1). The horizontal wind reached 107 m s^{-1}; a nearly 25 m s^{-1} updraft caused the instrument to rise ~200 m and remain suspended for about 90 s before resuming its regular descent. This measurement is in the upper 1% of measurements for the vertical wind (Black et al. 1996). When the descent resumed, the air temperature was about 1K cooler than at the

same level in the strong updraft, consistent with convective instability. During the time the instrument was suspended, the horizontal wind speed oscillated between ~70 m s^{-1} and 100 m s^{-1} at least three times, suggesting a strong rotational wind component on a much smaller scale than the axisymmetric mean circulation, i.e. an eyewall misocyclone.

A dual-airborne Doppler radar analysis was performed from NOAA P-3 tail radar data (Jorgensen et al. 1983) collected from 1749 – 1755 UTC, three minutes before and after the dropwindsonde release. A three-dimensional variational synthesis approach (Gamache et al. 1995) was used with 1.5 km and 0.5 km grid spacing in the horizontal and vertical, respectively, and a single-step Leise scale filter (Leise 1982) was applied to the final wind field. The Doppler synthesis inherently smooths the derived wind both temporally and spatially, particularly vertical velocity. The analyzed reflectivity, wind speed, vorticity, and vertical velocity at 1 km altitude are shown in Figure 5.2, strongly supporting the reliability the dropwindsonde measurements. A broad swath of horizontal wind speed exceeding 90 m s^{-1} is evident in the eyewall; strong radial shear of the horizontal wind with a peak vorticity of $15x10^{-3}$ s^{-1} is found on the inner edge of the eyewall near the aircraft track, upwind of a Doppler-derived 5 m s^{-1} updraft. The dropwindsonde may have been released into this particular feature as it was advected cyclonically along the inner edge of the eyewall.

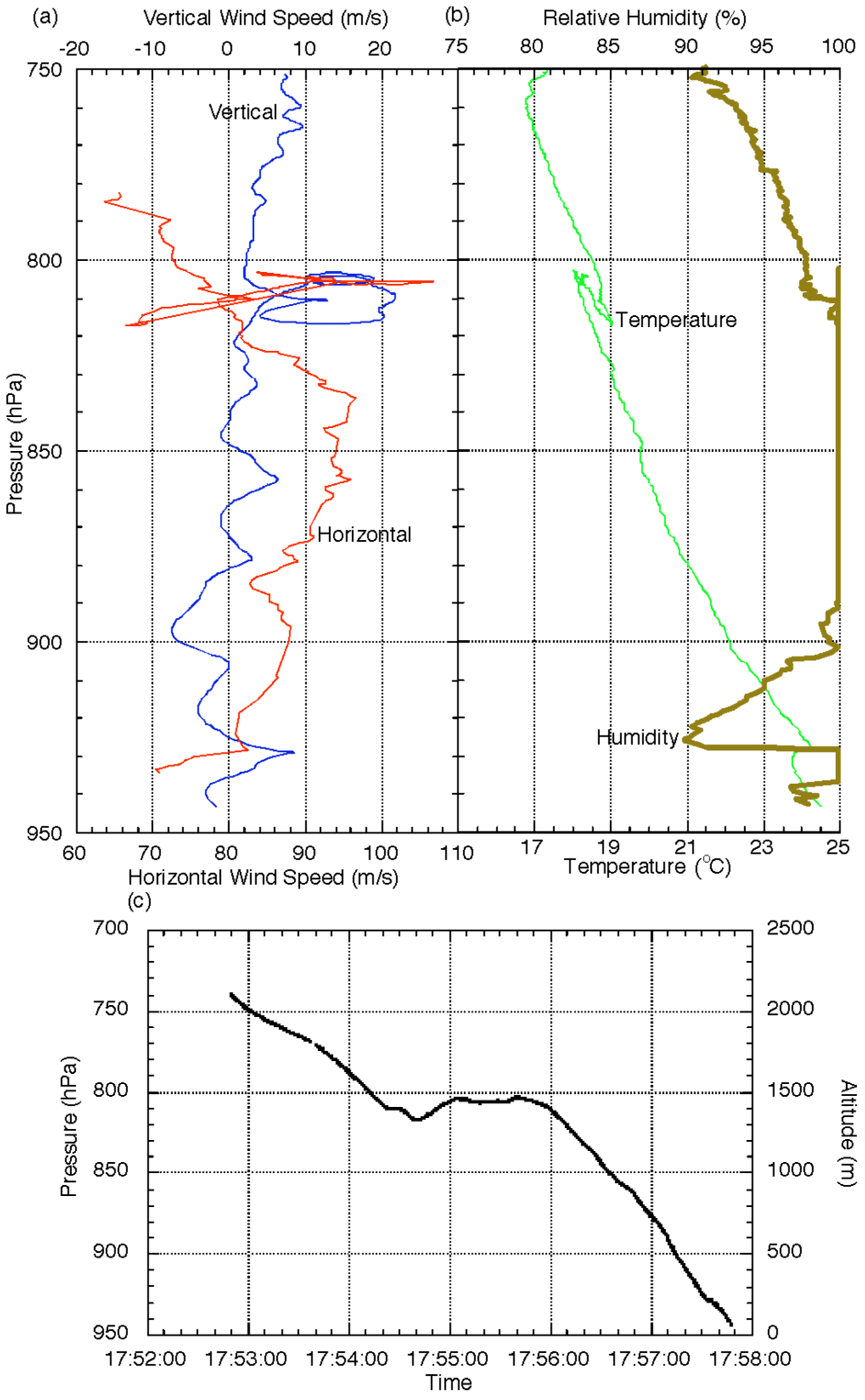

Figure 5.1: Data obtained by the dropwindsonde released inside the inner edge of the eyewall of Hurricane Isabel at 1752 UTC 13 September 2003: (a) horizontal and vertical wind speeds as a function of pressure, (b) temperature and relative humidity as a function of pressure, and (c) altitude and pressure as a function of time. [From Aberson et al. 2006]

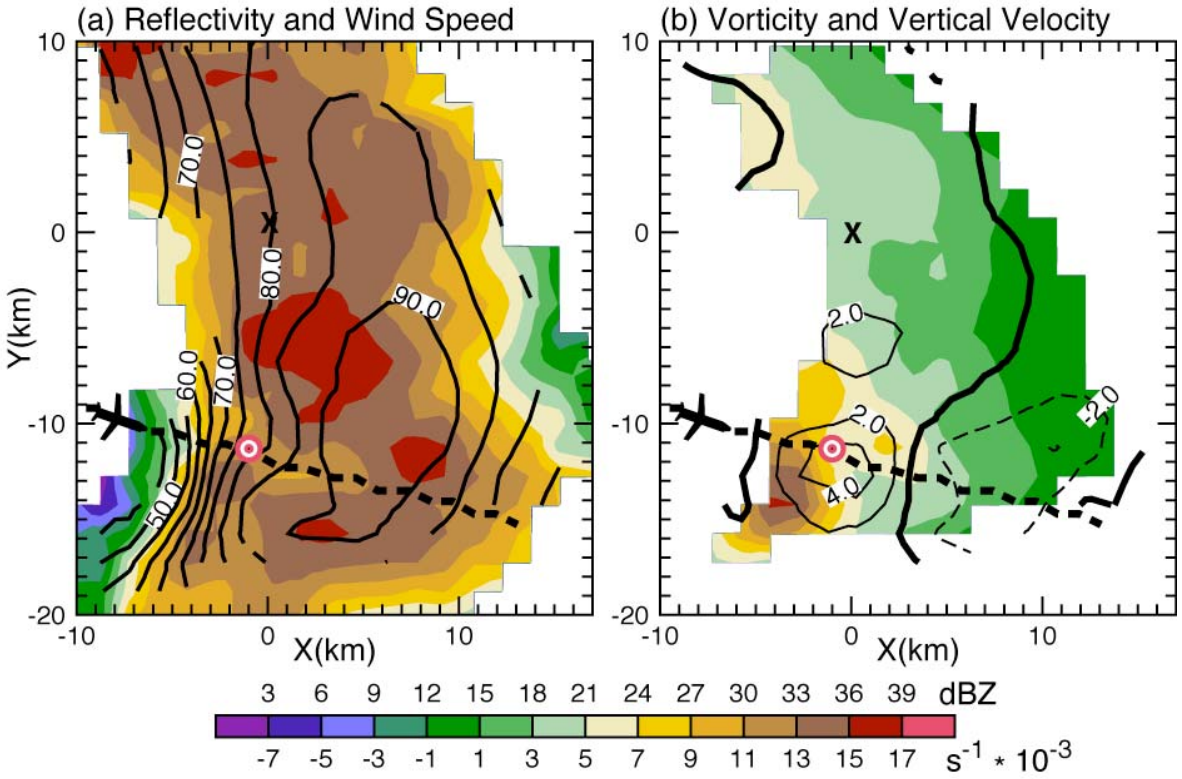

Figure 5.2: Dual-airborne Doppler analysis from NOAA P-3 tail radar at 1 km altitude at 1749-1755 UTC 13 September 2003: (a) average reflectivity from fore and aft scans in color (dBz) and contoured horizontal wind speed (m s^{-1}), and (b) contoured vorticity (*$10^{-3}s^{-1}$) and vertical velocity (m s^{-1}) in color (thin solid, thick solid, and dashed contours indicate upward motion, zero, and downward motions, respectively). In each panel, the dashed line shows the aircraft flight track during the analysis period; the bullseye indicates the dropwindsonde release location; and the origin (0, 0) indicated by an 'X' is the location of the record wind speed observation ~2.5 min after the dropwindsonde release.

The dropwindsonde measured wind in Hurricane Isabel associated with an eyewall misocyclone that are significantly stronger than the “superintense” wind of the mean vortex. The θ_e in the feature is about 5 K higher than that in the eyewall itself (not shown) suggesting either a mixing of air between the very high entropy eye and the lower entropy eyewall or that the air sampled originated below the eyewall after it gained entropy from surface flux.

Figure 5.3 shows fingers of high reflectivity extending from the eye into the

eyewall, and other cellular reflectivity maxima inside the inner edge of the eyewall at about the dropwindsonde release time. These features can be tracked in subsequent radar sweeps and are calculated to be rotating along the inner edge of the eyewall at roughly 70-80 m s^{-1}, coinciding approximately with the mean observed low-level wind speed. The dropwindsonde was released into the feature marked in the figure, and suspended within it during the time of the extreme wind measurement. The filamentary features on the inner edge of the eyewall resemble horizontally-aligned small-scale Kelvin-Helmholtz instability that feed off the kinetic energy of the intense cyclonic shear region in the inner edge of the eyewall. Similar vortex-tube-like features, aligned in the vertical, also have been observed in the eyewall of Hurricane Erin (Aberson and Halverson 2005).

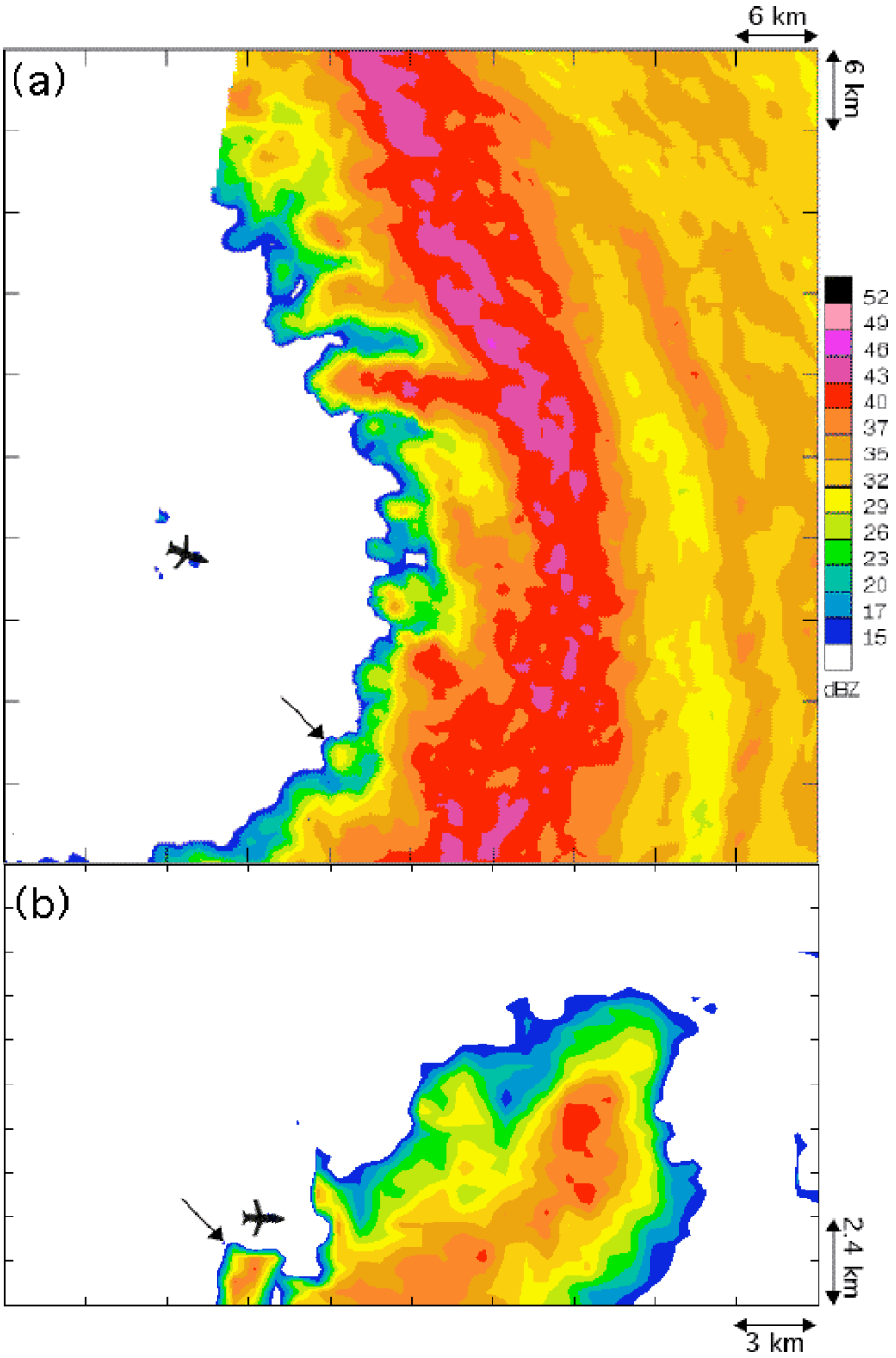

Figure 5.3: Radar reflectivity of the eastern eyewall of Hurricane Isabel. (a) close up single sweep of the NOAA WP-3D lower fuselage radar at 175035 UTC 13 September 2003 showing the filamentary features in the eastern eyewall. The arrow points to the feature the dropwindsonde sampled. The line shows the horizontal extent of (b) a single sweep close-up from the tail radar at 175250 UTC the same day showing the vertical structure of the sampled feature and the eyewall. In both panels, the aircraft symbol represents the P-3 location. [From Aberson et al. 2006]

Chapter 6

Analysis of Balance

6.1 Gradient wind balance

The full azimuthally averaged radial pressure equation in cylindrical coordinates is given by:

$$-\frac{\partial \bar{p}}{\bar{\rho}\partial r} = \left(-\frac{\bar{v}^2}{r} - f\bar{v} \right) + \frac{D\bar{u}}{Dt} + F \tag{6.1}$$

$$F = -(\overline{v'^2})/r + \partial(\overline{ru'^2})/r\partial r + \partial(\overline{u'w'})/\partial z \tag{6.2}$$

$$D\bar{u}/Dt = \partial\bar{u}/\partial t + \bar{u}\,\partial\bar{u}/\partial r + \bar{w}\,\partial\bar{u}/\partial z \tag{6.3}$$

where F represents eddy fluxes and friction; Du/Dt is the material derivative of the radial wind; u, v, and w are the cylindrical velocity components; t is time; f the Coriolis parameter, assumed constant; p the total pressure, ρ the total density; the overbar represents the azimuthal average; and primes represent perturbation components. Equation (6.1) can be integrated radially using a given wind field to obtain the estimated contributions from each term to the overall pressure deficit. Since F is unknown, it can be estimated by a residual given the observed pressure gradient.

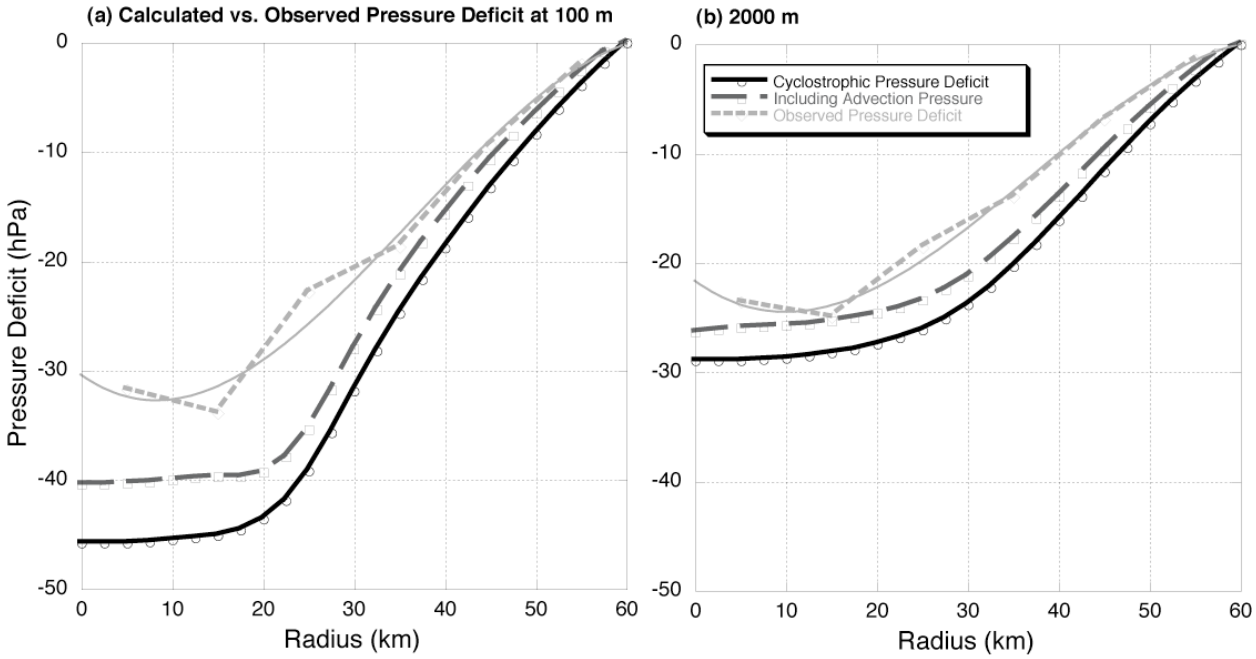

Figure 6.1: Calculated pressure deficit obtained by integrating the radial pressure equation (Eqn 4.1) inward from 60 km radius with (dark gray dashed curve) and without (black solid curve) advection (Du/Dt) terms, versus the pressure deficit observed by dropwindsonde data (light gray dotted curve) at (a) 100 m altitude and (b) 2 km altitude. Third degree polynomial fits (light gray thin curve) of the observed pressure gradient with R^2 values of (a) .98 and (b) .99 are also shown.

The results of this integration from composite wind data on September 13 are shown in Figure 6.1. An inward integration of Equation (6.1) using the composite winds with zero as the outer boundary condition at (a) 100 m and (b) 2 km altitude is compared to the observed pressure gradient. The integration was performed with only the cyclostrophic terms (black solid curve) and with the advection terms (*Du/Dt*) (gray dashed curve). The observed gradient was calculated by averaging dropwindsonde data in 10 km radial and 50 m vertical bins (dotted curve). This figure shows the importance of the *Du/Dt* term and relatively significant contribution from the residual terms in the boundary layer. The transverse advection pressure and eddy/friction act together to oppose the cyclostrophic terms and reduce the radial pressure gradient. These terms increase the central pressure by ~6 hPa and ~8 hPa, respectively. While some of the

residual may be due to uncertainties in the estimated axisymmetric central pressure, this term is roughly of the same order and sign as the advection terms in the boundary layer. At 2 km, the three curves parallel each other closely, consistent with a decrease in radial accelerations and eddy momentum fluxes. A small contribution from the residual terms is seen at all radii, but the central pressure deficit discrepancy is only a few hPa. This suggests that the vortex is roughly in gradient balance above the boundary layer on the 13th.

Alternatively, one can calculate the gradient wind from the observed pressure field. The last two terms in (6.1) are identically zero for a steady-state vortex in gradient wind balance, yielding a quadratic equation that can be solved for the gradient wind (Vg) given a known radial pressure distribution. To compute the gradient wind, the binned pressure data was fit to a 3rd degree polynomial (Fig 6.1a and b, thin solid line) and an analytic derivative was obtained. This derivative was then substituted into 5.1 and solved, yielding a simplified radial profile of the gradient wind (Fig 6.2a). While modeling the gradient wind as a quadratic function is clearly oversimplification, one can still gather qualitative estimates of super/sub-gradient winds in Isabel's inner core. From Figure 6.2a, the presence of supergradient winds around the eyewall region (r > 20 km) at low-levels (~100 m) is consistent with the inward deceleration of the radial flow (Smith, 1980). The simple quadratic function falls off too rapidly at outer radii, but suggests that the wind was ~20% supergradient near the RMW.

The transition from super- to subgradient winds occurs at ~20 km radius and is concurrent with a reverse in the radial acceleration near the center of the eye. This pattern is remarkably similar to a simple model for unbalanced flow constructed in Willoughby

(1990), shown in Fig 6.2b. Willoughby's model used a simple log-spiral inflow to model the radial wind, but the picture near the RMW is qualitatively similar to the results from Isabel. The radial acceleration terms act like an extra pressure, slowing down the tangential wind in the eye and speeding it up in the eyewall. At 2 km altitude, the TC is much closer to gradient wind balance, and the diagnosis as to the degree of super/sub-gradient winds using the simple, quadratic *Vg* was inconclusive (not shown).

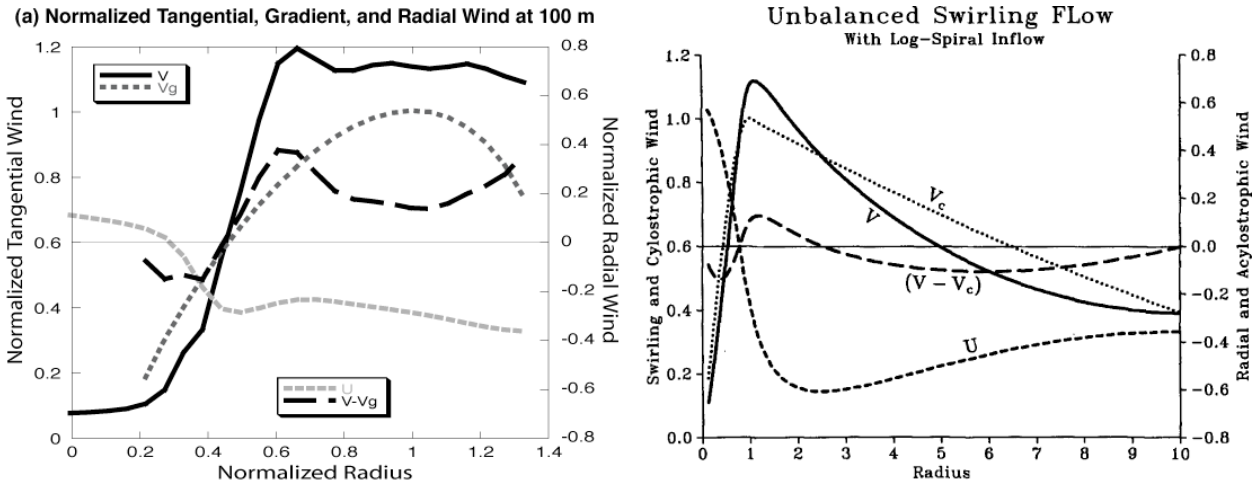

Figure 6.2: (a) Composite wind at ~100 m (0 – 250 m composite level) from Hurricane Isabel on 13 September, and (b) calculated nonbalanced wind in a cyclostrophic vortex with specified inflow angle such that the radial wind converges asymptotically to 0.8 times the radius of maximum cyclostrophic wind [from Willoughby 1990]. The dotted curve represents the cyclostrophic, or gradient wind, the solid curve the nonbalanced tangential wind, the shorter dashed curve the radial wind, and the longer dashed curve the difference between the balanced and nonbalanced wind. Wind components are nondimensionalized with the maximum balanced wind, and radius is nondimensionalized with the radius of maximum balanced wind.

6.2 Thermal wind balance

It is informative and useful to investigate whether the deduced mean tangential wind and entropy fields presented in Figure 4.1 and 4.2 are dynamically consistent. A

thermal wind equation relating the maximum mean tangential wind and the radial gradient of moist entropy at the top of the boundary layer has been derived previously (Emanuel 1986, Eq. 13; Emanuel 1997, Eq. 13):

$$V_m^{\,2} \approx -r_m (T_B - T_O) \frac{dS_B}{dr} \tag{6.4}$$

where S_B is the moist entropy at the boundary layer top, r is the radius from the vortex center, r_m is the RMW, V_m is the maximum mean tangential wind, and other symbols are as defined above. Equation (6.4) is a diagnostic equation whose validity depends on the hydrostatic and axisymmetric cyclostrophic balance approximations (Holton 2004) in the eyewall region of the storm. Cyclostrophic balance is a valid first approximation in the eyewall above the boundary layer where the Rossby number is large compared to unity and the flow is rotationally dominant (e.g., Willoughby 1990). As shown in the previous section, this assumption is fairly well satisfied for Isabel. The superintensity mechanism will of course alter the radial gradient of S_B (and thus the radial gradient of θ_e) and increase the resulting tangential wind speed. Therefore, (6.4) should be valid for superintensity as long as the winds are not appreciably supergradient, which appears to be a relatively valid assumption at 1 km. Since all quantities appearing in (6.4) are calculable from the data, we can use the data to assess the consistency of the thermal wind constraint, and conversely to determine if the outflow temperature computed in Section 7.2 is sufficiently cold to support the intense winds observed. From the θ_e data, one obtains the following approximate radial moist entropy gradient near r ~42 km (RMW) and z = 1 km (boundary layer top):

$$\frac{dS_B}{dr} = \frac{c_p}{\theta_e}\frac{d\theta_e}{dr}$$

$$\approx \frac{1004 J/kgK}{357 K}\cdot\left(\frac{-6k}{10km}\right)$$

$$= -1.7\times10^{-3}\frac{m}{s^2 K}.$$

(6.6)

Substituting this result into (3), using the values of T_B and T_O computed previously, yields $V_{\max} \approx 74\, ms^{-1}$. This is close to the observed $V_{\max}$ of $76\, ms^{-1}$ deduced from the dropwindsondes. If we instead use the observed $V_{\max}$ of $76\, ms^{-1}$ and infer the required outflow temperature to support this wind speed, for the above radial entropy gradient near the RMW, we obtain T_O = 216 K. This is close to the outflow temperature calculated from the dropwindsonde and the Gulfstream-IV data as described in Section 7.2.

It should be noted that this outflow temperature estimate is sensitive to the value chosen for the radial θ_e gradient. Errors from humidity sensor biases and spatial and temporal averaging limit the accuracy of the calculated radial entropy gradient. Deviations from axisymmetric thermal wind balance (6.4) near the boundary layer top are also expected due to the strong mesovortices observed near the RMW. Given all of these potential errors, we are encouraged by the consistency between the outflow temperature, the maximum tangential wind and radial entropy gradient on the 13th.

Similar calculations as to the degree of thermal wind balance on the 12th and 14th were also performed. These are summarized in Table 6.1. These results indicate rough agreement on the 14th, but the entropy gradient appears too weak for the given wind speed and outflow temperature. The discrepancy of ~1 K/10 km is within the range

of uncertainty for this measurement, however. The sensitivity to this slight discrepancy is apparent in the other two calculations, yielding a 30 degree shift in outflow temperature or 10 m s^{-1} decrease in the tangential wind for exact axisymmetric thermal wind balance. A more distinct discrepancy is shown between the wind and entropy fields at the RMW on 12 September. Due to uncertainties in the derived entropy gradient and calculated outflow temperature, it is difficult to assert with confidence that the storm was significantly unbalanced in this regard. However, the steeper entropy gradient at this radius (25 km) and the apparent balance at the larger RMW (45 km) by the next day suggest that some adjustment towards thermal wind balance may have taken place. With the limited temporal continuity and above mentioned uncertainties, further speculation is difficult.

12 September, 25 km RMW	T_O = -65 ˚C	$d\theta_e/dr$ = -5 K/ 10 km
V_m= 80 m s^{-1}	*$d\theta e/dr$ = -10.2 K/ 10 km*	*T_O = -158 ˚C*
T_O = -65 ˚C		*V_m = 56 m s^{-1}*
13 September, 45 km RMW	T_O = -58 ˚C	$d\theta_e/dr$ = -6 K/10 km
V_m= 76 m s^{-1}	*$d\theta e/dr$ = -5.7 K/ 10 km*	*T_O = -57 ˚C*
T_O = -58 ˚C		*V_m = 74 m s^{-1}*
14 September, 50 km RMW	T_O = -56 ˚C	$d\theta_e/dr$ = -3.5 K/ 10 km
V_m= 74 m s^{-1}	*$d\theta e/dr$ = -4.7 K/ 10 km*	*T_O = -83 ˚C*
T_O = -56 ˚C		*V_m = 64 m s^{-1}*

Table 6.1: Results of thermal wind diagnostic from Eq. (6.4) for 12 - 14 September. Top row and first column values are observed quantities. Gray shaded cells show the results of calculating for the remaining parameter assuming the other two quantities are known.

Chapter 7

Maximum Potential Intensity Analysis

In E-MPI theory, the primary environmental parameters that are needed to calculate the

a priori MPI are 1) the sea surface temperature (SST) in the hurricane core, 2) the upper-level exhaust (outflow) temperature where parcels undergo radiational cooling to space, and 3) the ambient RH near the sea surface. These input parameters were calculated according to the definitions used in E-MPI theory (Emanuel 1986; Rotunno and Emanuel 1987; Emanuel 1995) using available data from the hurricane and its environment.

7.1 Sea Surface Temperature

The core SST (Figure 7.1) was estimated from a combination of pre-storm satellite imagery, ARGOS buoy data, and low-altitude aircraft radiometer measurements. Multiple satellite SST products (McMillin and Crosby 1984; Brown and Minnett 1999; Legeckis and Zhu 1997) compare well during the period (not shown), suggesting no bias was present in any of the retrievals. SSTs on the 12th had values near the inner core at ~28.5 C, and Isabel began to encounter even warmer water on the 14th, with the estimated SST at ~29 C. The pre-storm satellite derived temperatures are well validated by airborne radiometer measurements (Moss 1978) recorded on board the P-3 NOAA 43 aircraft at ~60 and ~120 m above sea level to the northwest of the storm center on the 14th.

The cool wake of Fabian is evident in the central region of the plot, corresponding to the IOP on the 13th. Hurricane Fabian passed through this same area ten days prior to Isabel, resulting in cooler water near Isabel's core region on this day than that found in the surrounding area. Low altitude airborne radiometer measurements taken in the rear of Isabel measured a reduction in SST by ~1 – 2 ˚C relative to satellite-derived SST estimates prior to Isabel's passage, yielding a 27 ˚C average SST near the storm core on the 13th. This reduction is believed to be caused by Isabel and the corresponding shear-induced turbulent upwelling from the cold thermocline (e.g., Emanuel et al. 2004). This negative feedback effect is not represented in E-MPI theory. In Sec. 7.5, estimates of the impact of *storm-induced* cooling on the intensity of Isabel are presented, providing upper and lower bound intensity estimates. For the *a priori* MPI estimates, a constant SST of 27.5 ˚C is employed to represent the average SST during Isabel's passage over Fabian's wake on 13 September[2]. It is also interesting to note that near surface temperature measurements from the dropwindsondes (not shown) imply a ~ 3˚C temperature deficit across the ocean-air interface, consistent with recent observations (Wroe and Barnes 2003; Cione et al. 2000).

[2] In E-MPI theory the SST under the eyewall is critical for maintaining the *maximum sustained* tangential wind. Here, the boundary layer air parcels spiraling inward toward the eyewall from the outer core region possessing relatively warm (~28 °C) SSTs are assumed to quickly lose their 'thermodynamic memory' and to adjust rapidly to local (~27 °C) SST conditions on a boundary layer 'eddy-turnover' time scale τ ~ H/w', where H is the characteristic depth of the boundary layer and w' is a root-mean-square eddy vertical velocity. Letting H ~1 km and w' ~ $2\,ms^{-1}$ gives τ ~ 500 s ~ 8 min, a short time interval compared to that required for a boundary layer parcel to traverse horizontally inwards from the outer-core to the eyewall (L/U ~ 200km/$10\,ms^{-1}$ ~ 5 h, where L represents a typical distance between the outer-core and eyewall, and U is an upper bound to the average radial inflow within this region).

Figure 7.1: SST derived from AVHHR satellite (average SST over 04 to 10 September in color), and NOAA WP-3D downward-pointing radiometer (thin line, from ~18Z 13 and 14 September). Tracks of Hurricanes Fabian (dashed best track, from 02 to 05 September) and Isabel (dashed best track, with thick white, solid line indicating analysis periods from 16 – 23Z on 12 to 14 September) are shown for reference.

7.2 Outflow temperature

Individual soundings in the hurricane environment were used to calculate the outflow temperature. Though the MPI calculation is not very sensitive to the exact value used in the calculation, the broad range of possible values still make this an important parameter to calculate explicitly. The sounding locations used for the E-MPI calculation overlaid on infrared satellite imagery indicating the extent of the upper-level outflow on 13 September is shown in Figure 7.2.

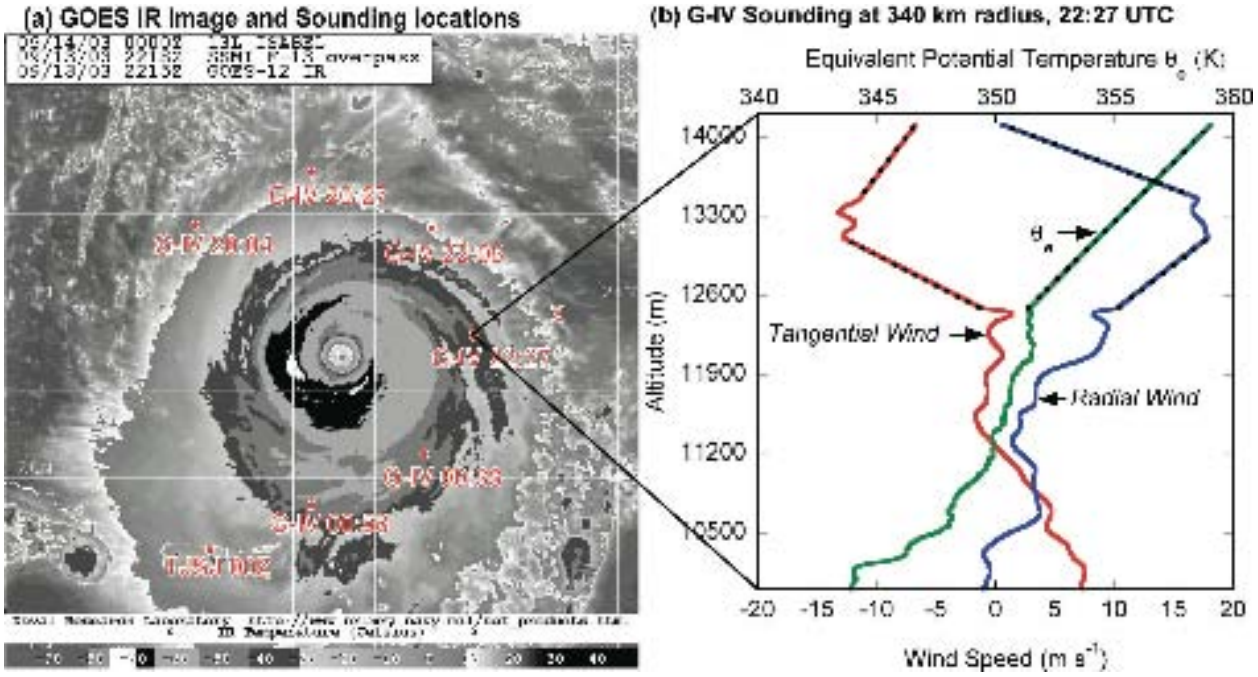

Figure 7.2 (a) GOES infrared satellite imagery at 2215 UTC (courtesy of NRL/Monterey) showing extent of hurricane outflow, and the dropwindsonde profile locations (red dots with UTC time labels) used in outflow temperature calculation. 'X' indicates location of additional outflow jet sample at 553 km radius from center, (b) High altitude wind speed (ms^{-1}) and θ_e (K) from NOAA Gulfstream-IV dropwindsonde at 341 km radius from center at 2227 UTC. Tangential (red) and radial (blue) winds show anticyclonic outflow, with θ_e in green. Black dashed line indicates linearly interpolated data.

Without the ability to track individual air parcels through eyewall ascent and into the outflow, the outflow temperature calculation requires some modification from previous studies with numerical models (Persing and Montgomery 2003; Rotunno and Emanuel 1987). The outflow temperature is calculated here in *three different ways:* as a *dln(θ_e)*-weighted temperature following the original definition in Emanuel (1986); as an equilibrium-level temperature (the temperature at which a virtual parcel starting from ambient surface state achieves the same environmental temperature after lifting by pseudo-adiabatic ascent); and as a radial-wind-weighted temperature across the storm outflow (Persing and Montgomery 2003). This last approach provides perhaps the most

empirical of the three calculations, in that it is a direct sampling of the radial outflow of the storm. Its deficiency with observational data is that the outflow is asymmetric and often concentrated in jets, thus uneven sampling may bias the estimate. The second may be considered the most physical, in that parcels which rapidly ascend in the eyewall must return to a level of neutral buoyancy as they recede from the storm, cooling gradually and sinking at large distances. The equilibrium level of a particular sounding depends heavily on the surface characteristics however, and may thus be biased if these characteristics are significantly different than that found in the hurricane environment, (i.e. if the sounding was taken over land instead of ocean.) The third calculation is unique to the E-MPI formulation, and is based on the Carnot engine concept. The E-MPI theory uses the $d\ln(\theta_e)$-weighted integral definition:

$$T_{out} \equiv \frac{1}{\ln\left[\frac{\theta_{ec}}{\theta_{ea}}\right]} \int_{\theta_{ea}}^{\theta_{ec}} T d\ln(\theta_e), \tag{7.1}$$

where θ_{ea} and θ_{ec} denote the ambient sub-cloud layer θ_e and that of a parcel in the eyewall updraft core (r ~ 45 km, see Figure 3b), respectively (Emanuel 1986; Rotunno and Emanuel 1987), consistent with the single-cycle Carnot model. Since θ_e is approximately conserved during ascent in the eyewall and in the upper-tropospheric outflow, $d\ln(\theta_e)$ is approximately zero until a parcel begins its descent due to radiational cooling at large (> 300 km) radii. Assuming the sounding θ_e represents that of a family of parcels advected from the storm in the outflow, the integral in (7.1) can be performed on a single environmental sounding. A parcel at the outflow layer top with high θ_e descends and loses energy through radiational cooling, ultimately resulting in a reduced

θ_e at the outflow layer bottom; the θ_e at the outflow layer bottom is assumed to be equal to θ_{ea} (Emanuel 1986; Rotunno and Emanuel 1987). As an example, Figure 7.2b shows an observed outflow jet at ~ 340 km radius sampled by a dropwindsonde released by the NOAA Gulfstream-IV. Anticyclonic outflow is seen at 11.5 km altitude and extends up to ~14 km, with peak anticyclonic tangential and radial winds of 13 ms^{-1} and 17 ms^{-1}, respectively. The observed θ_e is assumed to increase monotonically with height across the outflow layer from 350 K to 359 K. This is supported by an additional measurement at ~550 km radius along the same radial (location indicated by an 'X' in Figure 5a), with peak outflow wind of ~12 ms^{-1} at 13.5 km altitude and similar thermodynamic structure (not shown). In contrast, most observations of the outflow around the storm have radial wind speed < 10 ms^{-1}, confirming that the hurricane outflow is a complex structure comprised of asymmetric outflow jets instead of the broad and homogeneous exhaust system predicted in axisymmetric numerical models (e.g. Holland 1987; Flatau and Stevens 1989; Vladimirov et al. 2001). Note that the θ_e in the center of the outflow jet is 354 K, slightly less than that observed for the sub-cloud layer at the RMW (see Figure 4b), and approximately equal to the average θ_e across the eyewall base (cf. Houze 1993). These thermodynamic limits, from 350 K to 359 K, were used in the numerical integration of the seven environmental soundings[3] encircling the hurricane (Figure 7.2a,

[2] Missing data in the θ_e and wind fields were interpolated linearly between available observations in order to perform the integration. Though this smoothes the radial-wind in the Persing and Montgomery (2003) outflow proxy calculation, the monotonic $ln(\theta_e)$ profile is not sensitive to this.

Table 7.1). The arithmetic average of these seven temperatures is -58 ˚C and provides the primary system-scale outflow temperature[4] on the 13th.

Since the NOAA G-IV jet was not deployed on the 12th, a single radiosonde from San Juan provides an estimate of the outflow temperature on that day. The calculated outflow temperatures from this sounding are shown in the first row of Table 1. In this case, the radial wind weighted outflow (PM) and equilibrium level (EL) temperatures vary significantly from the $dln(\theta_e)$ weighted temperature (RE). The EL is near the tropopause, and seems unrealistically cold. The RE temperature of -65 C is reasonable however, and is consistent with the other two days, yielding a colder outflow than on the 13th or 14th due to higher θ_e limits used in the integral. Infrared satellite imagery provides a qualitative validation of this estimate, showing generally colder cloud top temperatures but no pixels below -75 C (Figure 7.3). Given the relatively good agreement on the 13th between the cloud top temperatures in the outer cloud shield (~350 km radius) and the calculated outflow temperatures, the -65 C estimate seems reasonable on the 12th. This single estimate results in an additional uncertainty in the *a priori* maximum mean tangential wind of 3 – 6 m s^{-1}, depending on the specific assumptions used in the calculation.

On the 14th, G-IV reconnaissance provides a comprehensive look at the ambient environment, allowing for a more robust calculation of the outflow temperature similar to 13 September. The bottom rows of Table 1 show a subset of the seven soundings used to

[3] The San Juan sounding appears to be an outlier. This could be due to the high tropopause height at low latitude, the high equilibrium level since the rawinsonde was launched from land, and/or the different sensor type from the GPS dropwindsondes.

compute the outflow on this day. The three methods described above yield similar estimates near -56 C. This also consistent with the value calculated on the 13th when the storm had similar thermodynamic structure at the eyewall, and with the apparent decrease in cloud top heights as seen in Figure 7.3b.

Figure 7.3: GOES infrared satellite imagery (courtesy of NRL/Monterey) at (a) 12/2045 UTC and (b) 14/2145Z showing extent of hurricane outflow, and the dropwindsonde profile locations (red dots with UTC time labels) used in outflow temperature calculation.

							Radial Outflow Layer			
Sounding	Radius from center (km)	RH (%)	T_B (^oC)	T_o PM (^oC)	T_o EL (^oC)	T_o EMPI (^oC)	θ_e Bottom (K)	Altitude Bottom (m)	θ_e Top (K)	Altitude Top (m)
TJSJ 12th 24:00:00 (SW)	861	82	21.4	-54.5	-58	-64.6	351.6	12420	363.0	15030
G-IV 13th 22:27:14 (NE)	341	72.6	24.9	-54.2	-59	-52.9	349.7	11140	358.8	14060
G-IV 13th 20:04:13 (NW)	525	82.5	24.5	-43.4	-44	-54.4	349.7	11700	354.9	13210
G-IV 13th 00:33:36 (SE)	347	77.7	23.8	-55.7	-50	-56.5	349.8	12090	359.2	14359
TJSJ 13th 24:00:00 (SW)	584	84.2	24.3	-70.7	-78	-79.5	349.7	14109	359.2	16539
Average of 7 soundings on the 13th	653.8	80.7	24.1	-52.9	-56.7	-57.8	349.7	12389	358.0	14801
G-IV 14th 20:04:42 (NE)	607	81.0	24.3	-51.2	-47	-56.2	349.8	11860	357.8	13470
G-IV 14th 19:21:57 (NE)	371	83.9	24.0	-45.8	-52	-51.3	349.7	11520	357.5	13290
G-IV 14th 18:36:44 (SE)	726	72.9	24.4	-47.1	-48	-61.5	349.7	12280	359.3	13770
TJSJ 14th 24:00:00 (SW)	726	71.8	23.2	-39	-61.2	-49.9	349.7	11079	359.3	14009
Average of 7 soundings on the 14th	609.7	81.9	24	-50.3	-49.4	-55.5	349.8	12038	358.0	13643

Table 7.1: Observed and calculated environmental temperatures and RH for Hurricane Isabel from 12 -14 September 2003**.** RH is the average in the lowest 500 m. Temperature at the boundary layer top (T_B), radial-wind-weighted outflow temperature

(T_O PM), equilibrium-level outflow temperature (T_O EL), $dln(\theta_e)$-weighted outflow temperature (T_O EMPI), and θ_e at the outflow layer top and bottom are also shown.

7.3 Relative humidity

The average RH over the lowest 500 m in these seven environmental soundings is near 80%, consistent with the boundary-layer mean structure (Figure 4.4b). In the original and revised *a priori* E-MPI formulations (Emanuel 1986; Emanuel 1995), a simple closure is invoked for the RH between the environment and the region under the eyewall by assuming a constant RH between these regions. Clearly, the near-saturated conditions throughout the sub-cloud layer underneath the eyewall violate this assumption. However, E-MPI also assumes that the air temperature is isothermal as it travels into the storm. The observed cooling tends to offset the moistening, yielding a similar effect in the moist entropy (e.g., Camp and Montgomery 2001). Thus, for the present calculations, a simple compromise is adopted (Emanuel 1995; Persing and Montgomery 2003), and a constant 80% RH is used.

7.4 Bulk Enthalpy and Momentum Exchange Coefficients

For the main intensity estimate, the ratio of bulk enthalpy and momentum exchange coefficients is assumed to be unity (C_K/C_D =1). Observational data collected during the 2002-2004 CBLAST field program suggests a value of unity is an upper bound; current estimates of this exchange ratio for near-surface (~10 m) hurricane force wind speeds vary from approximately 0.5 to 0.7 as shown in Figure 7.4 (Black et al. 2006). Direct measurements were obtained in minimal hurricane force winds however,

due to the inherent difficulty and danger in collecting airborne near-surface measurements at higher wind speeds. A photograph of the sea surface at hurricane force winds taken during the low-level (~60 m altitude) passes on the 13th is shown in Figure 7.5. Wind streaks and waves of varying size and age make parameterizing this complex structure challenging, to say the least.

At even higher wind speeds, laboratory tank experiments by Donelan et al. (2004) suggest that C_D reaches a limiting value as flow separation takes place. Direct observations of the enthalpy flux at extreme wind speeds have not yet been made. In Figure 7.4 the C_K/C_D ratio at 70 m s-1 is found from calculating a budget residual by Ramstrom and Emanuel (2004), suggesting a shift in the behavior of the enthalpy exchange coefficient at extreme wind speeds. One must be careful in interpreting these results however, since the ratio is calculated using a different method than the direct turbulent flux measurements obtained by the P3 aircraft. Given that the budget method calculates an effective C_E (or C_K)/C_D ratio, the radial flux of moist entropy from the eye may be implicitly accounted for in this estimate. The effects of sea spray on surface fluxes at wind speeds above 30 m s-1 are still poorly understood, but likely play a critical role in the air-sea interaction in major hurricanes (Fairall et al. 2003). Continued research on air-sea fluxes needs to continue in order to refine our estimates of these important parameters (e.g., Black 2004; Sullivan et al. 2004a, b).

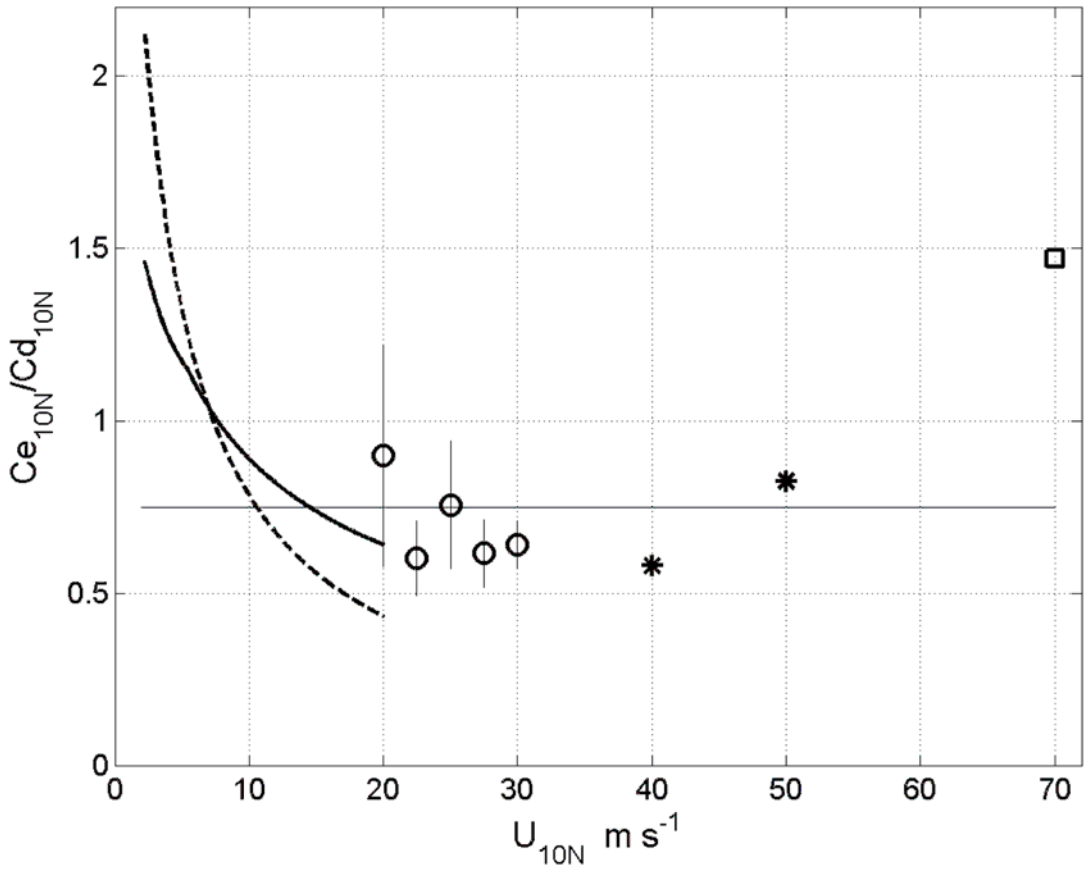

Figure 7.4: Ratio of Dalton number (enthalpy exchange coefficient) to drag coefficient derived from CBLAST measurements (circles with vertical lines indicating standard error) as well as an average of prior values below 20 m/s from HEXOS (DeCosmo et al., 1996; Smith et al, 1992, dashed line) and TOGA-COARE 3.0 (Fairall et al 2003, solid line). Estimated value based on budget estimate (Emanuel, 2004) at winds near 70 m/s is shown with a square. Interpolated estimates from Fairall estimate of spray effects shown with asterisks. The thin horizontal line is the 0.75 threshold for TC development proposed by Emanuel, 1996. [From Black et al, 2006]

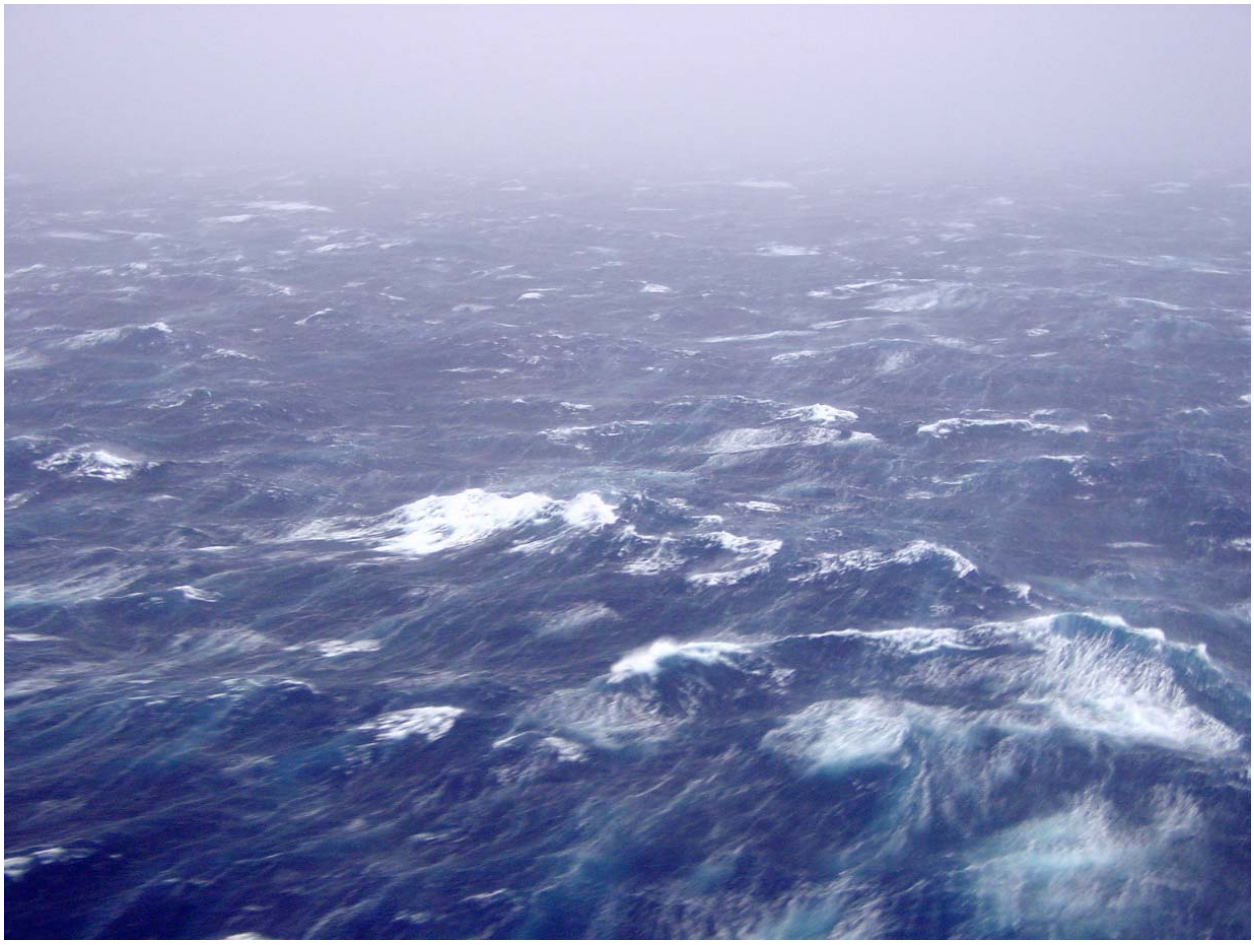

Figure 7.5: Photograph of sea surface in Hurricane Isabel taken from NOAA 43 during stepped descent pattern at 60 m altitude. Surface wind speed is 20 – 30 m s-1 [Photo courtesy Michael Black]

7.5 MPI estimates: Azimuthal mean V_{max} at boundary layer top

Figure 7.6 shows the predicted V_{max} from the *a priori* E-MPI theory for varying outflow temperatures and near-core SSTs with a constant RH = 80%. In this calculation T_B is assumed to be ~4 ˚C cooler than the SST, as suggested by the observational data in Table 7.1, and the thermodynamic efficiency is defined by Eq. (2.1). The average efficiency for Isabel on 13 September with an SST of 27.5 ˚C is found to be 0.275. This is the *original* definition of the efficiency of the Carnot cycle (Emanuel 1986), and provides a clear distinction between the SST and the air temperature at the top of the

boundary layer (e.g., Houze 1993). The predictive formula used here for V_{max} is otherwise identical to a revised formulation of the Carnot model (Emanuel 1995) and is the basis for the values shown in Figure 7.6.

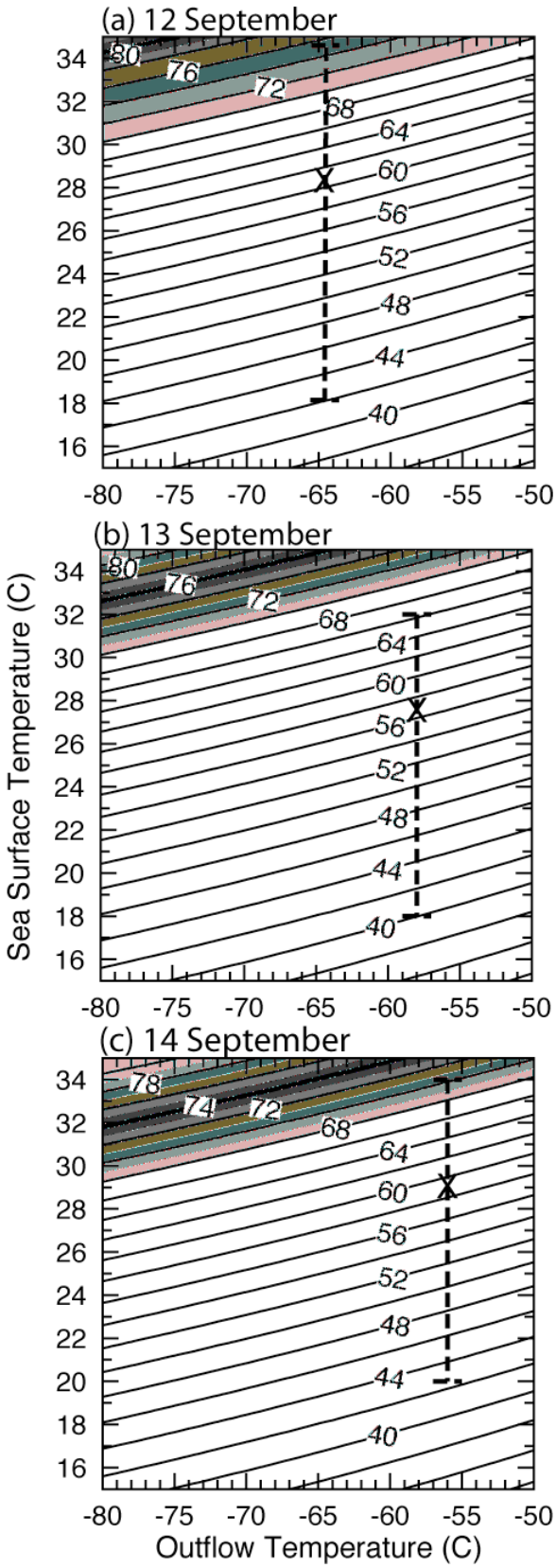

Figure 7.6. Theoretically predicted azimuthal mean V_{max} at the boundary layer top for varying outflow temperature and near-core SST with a constant RH = 80%. 'X' indicates the primary potential intensity estimate for the observed near environment around Isabel. The dark solid curve represents the average storm-relative tangential wind speed at the top of the boundary layer derived from the dropwindsonde measurements. The shading represents the standard deviation of this mean value. This a priori E-MPI estimate assumes C_K/C_D =1. See text for assumptions leading to upper and lower bound estimates.

The observed azimuthal mean tangential wind speed at the boundary layer top (76 ms^{-1}, with a 6 ms^{-1} standard deviation) on 13 September is clearly stronger than the theoretically predicted 56.6 ms^{-1} E-MPI. The effect of warm ocean eddies do not seem to be a plausible explanation for this discrepancy given that SST observations clearly depict the cool wake left earlier by Fabian (cf. Emanuel et al. 2004). Airborne radiometer measurements (Figure 7.1) and satellite data (not shown) and indicate that the SST was an additional 1-2 K lower in this region *after* the passage of Isabel, suggesting that other proposed intensity changes caused by the storm-induced ocean cooling (Emanuel et al. 2004) and turbulent dissipative heating (Bister and Emanuel 1998) tend in opposite ways.

The (turbulent) dissipative heating effect (Bister and Emanuel 1998) relative to the original *a priori* MPI (Emanuel 1986; Emanuel 1995) is calculated according to $\Delta(V_{max}) = V_{max}\left[\left(T_B/T_O\right)^{1/2} - 1\right]$, which for Isabel is a 9.6 ms^{-1} boost. Ocean cooling effects depend primarily on the storm translation speed and the oceanic mixed layer depth. Emanuel et al. (2004) predicted a ~13 ms^{-1} intensity reduction for a storm moving at 7 ms^{-1} with a 30 m mixed layer depth (their Sec. 2c, Fig. 3). Isabel had a similar translation speed but crossed the wake left by Fabian, and may have encountered a deeper mixed layer, resulting in a somewhat weaker cooling and reduced negative feedback effect. Figure 7.6 presents estimated upper and lower bounds for the maximum intensity in order to reflect uncertainties in both the bulk exchange ratio (C_K/C_D) and the storm-induced ocean cooling. The vertical dashed line presents a range of mean intensities employing the same outflow temperature, SST and RH used to obtain 'X' so as to reflect uncertainties in the bulk exchange ratio and the ocean cooling effect. The upper bound (~66 ms^{-1}) neglects entirely the ocean cooling, includes dissipative heating, and assumes

that $C_K/C_D = 1$. The lower bound (~40 ms^{-1}) assumes $C_K/C_D = 0.5$, and assumes the ocean cooling effect is compensated by the dissipative heating effect. The discrepancy between these predicted values and the observed intensity suggests a significant limitation of E-MPI theory.

Using a C_K/C_D value of one, and assuming the dissipative heating is entirely offset by the ocean cooling feedback, one achieves a theoretical MPI of 61.2 m s^{-1} for 12 September. This value is ~19 m s^{-1} below the observed mean tangential wind at the top of the boundary layer of 80 m s^{-1}. Using similar assumptions as on the 13th for the upper and lower bound estimates yields a range of 42 – 76 m s^{-1}. The highest value is within the standard deviation (10 m s^{-1}) of the mean tangential wind estimate in this case. This suggests that the superintensity mechanism may have played a role on the 12th as well, though perhaps not as dramatically as on the 13th. As was shown in Sec. 4.3, the boundary layer θ_e structure on the 12th conforms more closely to a more classic ("in-up-out") thermodynamic pathway, in which a substantial θ_e gain is achieved by a parcel spiraling in from the environment, and is augmented by strong surface fluxes at the eyewall. Additional high θ_e in the eye and the presence of eye and eyewall mesovortices suggest that the superintensity mechanism may be partially responsible for the storm exceeding the *a priori* MPI.

Warmer sea surface temperatures yields slightly higher MPI values on 14 September than those on the 13th, but weaker than that found on the 12th. Using the same assumptions for the upper and lower bounds yields a range of 42 – 69 m s^{-1}, with a best estimate of 59.0 m s^{-1}. The MPI is therefore exceeded on this day as well, in which the maximum value of θ_e in the eye is diminished but the overall area of the potential entropy

reservoir increased as compared to the previous day. While the size of the eye likely plays an important role in determining the available energy for the system, it is unclear at this point how much of that energy is able to accessed by the hurricane.

Chapter 8

Conclusions

A rigorous analysis of the structure, evolution, and MPI of Hurricane Isabel near its maximum intensity was performed using a combination of dropwindsonde, flight-level, and satellite data. This analysis reveals a nearly steady-state, expanding tangential wind field accompanied by dramatic changes in the secondary circulation and moist entropy structure. A distinct increase in radial inflow, vertical velocity, and low-level theta-e in the eye from the 12^{th} to the 13^{th} suggests a build-up of moist entropy due to latent heat fluxes in the relatively quiescent, low-pressure eye which is then accessed by parcels that are able to penetrate the eyewall, via the intense low-level inflow or mixing associated with mesovortices. The injection of this heat energy into the eyewall supports the strengthening of the secondary circulation, both in an axisymmetric sense and as a local buoyancy source (Eastin, 2004), resulting in, or possibly concurrent with, increased advection of higher momentum air from the outer core and expansion of the wind field. Despite encountering a cooler SST, Isabel maintained 76 ms-1 winds and expanded during this period.

The inner core Rossby-Ertel potential vorticity structure of Isabel obtained through the Barnes analysis provides a new look at the details of this important dynamical quantity in a category 5 hurricane. Significant vorticity ($> 6 * 10^{-3}$ s^{-1}) and potential vorticity (>60 PVU) are found at the inner edge of the eyewall on each day, with a pronounced ring structure typically associated with very intense vortices. This

ring, or bowl, of high PV supports the necessary condition for barotropic instability, which has been shown to be a probable mechanism for producing hurricane mesovortices and polygonal eyewalls (Schubert et al. 1999, Kossin and Schubert, 2005). This breakdown of the vortex sheet allows for mixing at the eye/eyewall interface and penetration of the high inertial stability of the eyewall by inflowing parcels, providing a consistent dynamic mechanism for the thermodynamic augmentation of the hurricane engine described in this paper. A secondary PV maximum is found near 3 km altitude in the eye, coupled with a thermal inversion and decrease in relative humidity. This feature has been identified in a numerical simulation of an intense hurricane (Wang and Zhang, 2003), but its dynamical significance has not been explored thoroughly to the authors' knowledge. This remains a topic for further research.

An analysis of gradient wind balance suggests that the winds in the boundary layer were supergradient in the eyewall, but transitioned to subgradient inside the eye. This is consistent with the radial accelerations observed in the axisymmetric wind composite, and showed a radial structure that is strikingly similar to a simplified log-spiral inflow model from Willoughby (1990). At 100 m, the contribution from the radial advection and eddy/friction terms was significant, opposing the cyclostrophic pressure gradient and reducing the central pressure deficit by ~15 hPa. At 2 km, the observed pressure gradient and integrated pressure deficit agree well, indicating that the storm was near gradient balance above the boundary layer.

Thermal wind balance was difficult to assess using the dropwindsonde data due to the diagnostic equation's sensitivity to the radial gradient of moist entropy at the eyewall. Results suggested that the observed moist entropy gradient and outflow temperature were

relatively consistent with the maximum mean tangential wind on the 13th, but less so on the 14th. This analysis also revealed a distinct discrepancy in the observed radial entropy gradient from that calculated by the thermal wind relationship on the 12th. The steeper entropy gradient at the former RMW (25 km) and the apparent balance at the larger RMW (45 km) by the next day suggest that some adjustment towards thermal wind balance may have taken place, but limited temporal continuity and uncertainty in the entropy gradient and outflow temperature preclude further speculation as to the details of this adjustment process.

A detailed analysis and test of E-MPI theory using high resolution observational data of a category five storm has not been previously presented to the author's knowledge. This study suggests that Hurricane Isabel's structure and intensity was largely consistent with many of the central concepts of the E-MPI theory regarding boundary layer balance, and the hurricane as a Carnot engine. However, the evidence that Isabel exceeded the currently accepted MPI indicates that revisions to this important dynamical concept need to be addressed. The discrepancy between the *a priori* MPI theory and the observed structure is consistent with recent high-resolution numerical model predictions of Persing and Montgomery (2003), suggesting that Isabel was superintense as defined therein. This study provides further evidence that entropy production in the low-level eye provides an important and overlooked energy source for the hurricane engine, and challenges classic theories about the degree of moist entropy obtained from the ocean in the outer core and underneath the eyewall.

While the conclusions presented here are robust for this dataset, further research with additional case studies and numerical modeling is needed to elucidate the various

thermodynamic pathways available to the tropical cyclone for maintenance and growth. The relative importance of the size of the eye, the fraction of eye θ_e actually utilized by the hurricane, and the degree to which the superintensity mechanism is active in storms of varying intensity, are interesting and open questions for future research.

References

Aberson, S. D., and J. B. Halverson, 2005: Kelvin-Helmholtz waves in the eyewall of Hurricane Erin. Submitted to *Mon. Wea. Rev.*

Aberson, S.D., M.T. Montgomery, M. Bell, and M. Black, 2005: Superintense winds in hurricane Isabel (2003). Part II: Extreme wind speeds. *Bull. Amer. Met. Soc.*, accepted with minor revisions.

Barnes, S.L., 1973: Mesoscale objective analysis using weighted time-series observations. NOAA Tech. Memo. ERL NSSL-62, National Severe Storms Laboratory, Norman, OK 73069, 60 pp.

Beven, J. and H. Cobb, 2004: Tropical cyclone report on Hurricane Isabel (2003). National Hurricane Center/Tropical Prediction Center.

Bister, M. and K.A. Emanuel, 1998: Dissipative heating and hurricane intensity. *Meteor. Atmos. Phys.* **65**, 233 - 240.

Black, M. L., R. W. Burpee, and F. D. Marks, 1996: Vertical motion characteristics of tropical cyclones determined with airborne Doppler radial velocities. *J. Atmos. Sci.*, **53**, 1887-1909.

Black, P.G., 2004: An overview of CBLAST flights into hurricanes Fabian and Isabel (2003) *Preprints, 26th Conf. on Hurricanes and Tropical Meteorology*, 1 - 2.

-----, E. A. D'Asaro, W. M. Drennan, J. R. French, P. P. Niiler, T. B. Sanford, E. J. Terrill, E. J. Walsh and J. Zhan. Air-Sea Exchange in Hurricanes: Synthesis of Observations from the Coupled Boundary Layer Air-Sea Transfer Experiment. *Bull. Amer. Met. Soc.* submitted.

Braun, S. A., 2002: A cloud-resolving simulation of hurricane Bob (1991): Storm structure and eyewall buoyancy. *Mon. Wea. Rev.,* **130**, 1573–1592.

-----, M. T. Montgomery, and Z. Pu, 2005: High-resolution simulation of Hurricane Bonnie (1998). Part I: The organization of eyewall vertical motion. *J. Atmos. Sci., NASA/CAMEX special issue*, in press.

Brown, O.B., and P.J. Minnett, 1999: MODIS infrared sea surface temperature algorithm theoretical basis document, ver 2.0, http://modis.gsfc.nasa.gov/data/atbd/atbd_mod25.pdf.

Callaghan, R., and R. K. Smith, 1998: The relationship between maximum surface wind speeds and central pressure in tropical cyclones. *Aus. Meteor. Mag.* 47 (3): 191-202

Camp, P. and M.T. Montgomery, 2001: Hurricane maximum intensity: Past and present. *Mon. Wea. Rev*., **129**, 1704 – 1717.

Carrier, G. F., A. L. Hammond and O. D. George, 1971: A model of the mature hurricane. *J. Fluid Mech. Sci.*, 47, 145-170.

Cram, T. A., J. Persing, M. T. Montgomery, and S. A. Braun, 2005: A Lagrangian trajectory view on transport and mixing processes between the eye, eyewall and environment using a high resolution simulation of Hurricane Bonnie (1998). *J. Atmos. Sci.*, submitted.

Cione, J., P. Black, and S. Houston, 2000: Surface observations in the hurricane environment. *Mon. Wea. Rev*. **128**, 1550 - 1561.

DeMaria, M. and J. Kaplan, 1994: Sea surface temperatures and the maximum intensity of atlantic tropical cyclones. *J. Climate*, **7**, 1324-1334.

DeMaria, M., M. Mainelli, L.K. Shay, J.A. Knaff, and J. Kaplan, 2005: Further

Improvements to the Statistical Hurricane Intensity Prediction Scheme (SHIPS), *Wea. Forecasting*, **20**, 531-543.

Donelan, M. A., B. K. Haus, N. Reul, W. J. Plant, M. Stianssnie, H. C. Graber, O. B. Brown, E. S. Saltzman, 2004: On the limiting aerodynamic roughness of the ocean in very strong winds. *Geophys. Res. Lett.,* **31,** L18306.

Eastin, M. D., P. G. Black, and W. M. Gray, 2002: Flight-level instrument wetting errors in hurricanes. Part I: Obser vations. *Mon. Wea. Rev.,* **130,** 825–841.380.

-----, W.M. Gray, and P.G. Black, 2005: Buoyancy of convective vertical motions in the inner core of intense hurricanes. Part II: Case studies. *Mon. Wea. Rev*., **133**, 209 – 227.

Emanuel, K.A., 1986: An air-sea interaction theory for tropical cyclones. Part I: Steady-state maintenance. *J. Atmos. Sci.* **43**, 585 - 604.

-----, 1988: The maximum intensity of hurricanes. *J. Atmos. Sci.*, **45**, 1143 - 1155.

-----, 1991: The theory of hurricanes. *Annual Rev. Fluid Mech.,* **23**, 179-196.

-----, 1995: Sensitivity of tropical cyclones to surface exchange coefficients and a revised steady-state model incorporating eye dynamics. *J. Atmos. Sci*., **52**, 3969 – 3976.

-----, 1997: Some aspects of hurricane inner-core dynamics and energetics. *J. Atmos. Sci.*, **54**, 1014 - 1026.

-----, DesAutels, C., C. Holloway, and R. Korty, 2004: Environmental control of tropical cyclone intensity. *J. Atmos. Sci.* **61**, 843 - 858.

-----, 2005: Divine Wind, Oxford University Press.

Fairall, C. W., E. F. Bradley, J. E. Hare, A. A. Grachev and J. B. Edson, 2003: Bulk parameterization of air-sea fluxes: updates and verification for the COARE algorithm.

J. Climate, **16**, 571-591.

Flatau, M. and D.E. Stevens, 1989: Barotropic and inertial instabilities in the hurricane outflow layer. *Geophys. Astrophys. Fluid Dyn.,* **47**, 1 – 18.

Franklin, J., M. L. Black and K.Valde. 2003: GPS Dropwindsonde Wind Profiles in Hurricanes and Their Operational Implications**.** *Wea. Forecasting*. **18**, 32–44.

Gamache, J. F., F. D. Marks, and F. Roux, 1995: Comparison of three airborne Doppler sampling techniques with airborne in situ wind observations in Hurricane Gustav (1990). *J. Atmos. Oceanic Technol.,***12**, 171-182.

Hawkins, H.F. and D. T. Rubsam. 1968: Hurricane Hilda, 1964, II. Structure and budgets of the Hurricane on October 1, 1964. *Mon. Wea. Rev.* **96**, 617–636.

-----, and S. M. Imbembo, 1976: The Structure of a Small, Intense Hurricane—Inez 1966. *Mon. Wea. Rev.* **104**, 418–442.

Hock, T.F. and J.L. Franklin, 1999: The NCAR GPS dropwindsonde. *Bull. Amer. Met. Soc.,* **80**, 407 - 420.

Hobgood, J. S., 2003: Maximum Potential Intensities of Tropical Cyclones near Isla Socorro, Mexico. *Wea. and Forecasting*, **18**, 1129–1139.

Holland, G., 1987: *Global View of Tropical Cyclones,* Section 2.7. R. Elsberry, Editor.

Holland, G. J., 1997: The maximum potential intensity of tropical cyclones. *J. Atmos. Sci.,* **54,** 2519-2541.

Holton, J. R., 2004: *An Introduction to Dynamic Meteorology.* Academic Press.

Houze, R., 1993: *Cloud Dynamics.* Academic Press.

Jorgensen, D. P., P. H. Hildebrand, and C. L. Frush, 1983: Feasibility test of an airborne pulse Doppler meteorological radar. *J. Appl. Meteor.,* **22**, 744-757.

Kleinschmidt, E., 1951: Grundlagen einer Theorie der Tropischen Zyklonen. *Arch. Meteorol. Geophys. Bioklimatol.,* A4, 53-72.

Koch, S.E., M. Desjardins, and P.J. Kocin, 1983: An interactive Barnes objective map scheme for use with satellite and conventional data. *J. Climate Appl. Meteor.* **22**, 1487 – 1503.

Kossin, J.P., and W.H. Schubert, 2001: Mesovortices, polygonal flow patterns, and rapid pressure falls in hurricane-like vortices. *J. Atmos. Sci*. **58**, 2196 – 2201.

-----, and -----, 2004: Mesovortices in hurricane Isabel. *Bull Amer. Met. Soc.*, 151- 153.

Lee, W.-C. and F. D. Marks Jr.. 2000: Tropical Cyclone Kinematic Structure Retrieved from Single-Doppler Radar Observations. Part II: The GBVTD-Simplex Center Finding Algorithm. *Mon. Wea. Rev.,***128**, 1925–1936.

LeeJoice, R. N., 2000: Hurricane inner-core structure as revealed by GPS dropwindsondes. Department of Atmospheric Science Bluebook No. 477, 56 pp.

Legeckis, R. and T. Zhu, 1997: Sea surface temperatures from the GOES-8 geostationary satellite. *Bull. Amer. Met. Soc.*, **78**, 1971 - 1983.

Leise, J. A., 1982: A multidimensional scale-telescoped filter and data extension package. NOAA Tech. Memo ERL WPL-82, 19pp. [Available from NOAA, 325 Broadway, Boulder, CO
80303].

Malkus, J. S. and H. Riehl, 1960: On the dynamics and energy transformations in steady-state hurricanes. *Tellus*, **12**, 1-20.

Miller, B. I., 1958: On the maximum intensity of hurricanes. *J. Met.*, **15**, 184-195.

Montgomery, M.T., V. A. Vladimirov, and P.V. Denissenko, 2002: An experimental study on hurricane mesovortices. *J. Fluid. Mech.*, **471**, 1 – 32.

McMillin, L.M., and D.S. Crosby, 1984: Theory and validation of the multiple window sea surface temperature technique. *J. Geophys. Res.*, **89(C3)**, 3655 – 3661.

Moss, M.S., 1978: Low-layer features of two limited-area hurricane regimes. *NOAA Technical Report ERL 394-NHEML 1*, pgs 17-18.

Nolan, D. S., and M. T. Montgomery, 2002: Nonhydrostatic, three-dimensional perturbations to balanced, hurricane-like vortices. Part I: Linearized formulation, stability, and evolution. *J. Atmos. Sci.*, **59**, 2989–3020.

Persing, J. and M.T. Montgomery, 2003: Hurricane superintensity. *J. Atmos. Sci.* **60**, 2349 – 2371.

Pielke, R. Jr. and Christopher W. Landsea. 1998: Normalized Hurricane Damages in the United States: 1925–95**.** *Wea. and Forecasting*. **13**, 621–631.

Ramstrom W. D. and K. A. Emanuel, 2004: Surface fluxes at high wind speeds deduced from dense dropwindsonde deployments in Hurricanes Fabian and Isabel. *Presented 26th Conf. on Hurricanes and Tropical Meteorology.*

Rotunno, R., 1984: An investigation of a three-dimensional asymmetric vortex. *J. Atmos. Sci.*, **41**, 283 - 298.

----, and K.A. Emanuel, 1987: An air-sea interaction theory for tropical cyclones. Part II: Evolutionary study using a nonhydrostatic axisymmmetric model. *J. Atmos. Sci.* **44**, 542 - 561.

Schubert, W.H., M.T. Montgomery, R.K. Taft, T.A. Guinn, S.R. Fulton, J.P. Kossin, and J.P. Edwards, 1999: Polygonal eyewalls, asymmetric eye contraction, and potential vorticity mixing in hurricanes. *J. Atmos. Sci.*, **56**, 1197 - 1223.

----, 2004: A generalization of Ertel's potential vorticity to a cloudy, precipitating atmosphere. *Meteor. Z.,* **13**, 465–471

Shapiro, L. J., 1983: The asymmetric boundary layer flow under a translating hurricane. *J. Atmos. Sci.*, **40**, 1984 – 1998.

Smith, R. K. 1980: Tropical Cyclone Eye Dynamics. *J. Atmos. Sci.*, **37**, 1227–1232.

Sullivan, P., J. McWilliams, and W.K. Melville, 2004a: Impacts of break waves and Langmuir circulations on the ocean mixed layer in high winds. *Preprints, 26th Conf. on Hurricanes and Tropical Meteorology*, 54 - 55.

-----, ----- and ----- 2004b: The oceanic boundary layer driven by wave breaking with stochastic variability. I: Direct numerical simulations. *J. Fluid Mech.*, **507**, 143 - 174.

Tonkin, H., G. J. Holland, N. Holbrook, and A. Henderson-Sllers, 2000: An evaluation of thermodynamic estimates of climatological maximum potential intensity. Mon. Wea. Rev., **128**, 746-762.

Vladimirov, V.A., V.I. Yudovich, M. Yu Zhukov, and P.V. Denissenko, 2001: Asymmetric

flows induced by a rotating body in a thin layer. HIMSA Preprint, **3**, 45 pp.

Wang, J. 2005: Evaluation of the Dropsonde Humidity Sensor Using Data from DYCOMS-II and IHOP_2002. *J. Atmos. Ocean. Tech.*, **22,** 247–257.

Wang, X. and D.-L. Zhang. 2003: Potential Vorticity Diagnosis of a Simulated Hurricane. Part I: Formulation and Quasi-Balanced Flow**.** *J. Atmos. Sci.*, **60**, 1593–1607.

Willoughby, H.E., and M. B. Chelmow., 1982: Objective determination of hurricane tracks from aircraft observations. *Mon. Wea. Rev.*, **110**, 1298-1305.

----, 1990: Gradient balance in tropical cyclones**.** *J. Atmos. Sci.*, **47**, 265–274.

Wroe, D.R., and G.M. Barnes, 2003: Inflow layer energetics of Hurricane Bonnie (1998) near landfall. *Mon. Wea. Rev.* **131**, 1600 – 1612.

Zipser, E. J., R. J. Meitin, and M. A. LeMone, 1981: Mesoscale motion fields associated with a slowly moving GATE convective band. *J. Atmos. Sci.*, **38,** 1725–1750.